

Journal of Materials Chemistry A

Accepted Manuscript



This is an *Accepted Manuscript*, which has been through the Royal Society of Chemistry peer review process and has been accepted for publication.

Accepted Manuscripts are published online shortly after acceptance, before technical editing, formatting and proof reading. Using this free service, authors can make their results available to the community, in citable form, before we publish the edited article. We will replace this *Accepted Manuscript* with the edited and formatted *Advance Article* as soon as it is available.

You can find more information about *Accepted Manuscripts* in the [Information for Authors](#).

Please note that technical editing may introduce minor changes to the text and/or graphics, which may alter content. The journal's standard [Terms & Conditions](#) and the [Ethical guidelines](#) still apply. In no event shall the Royal Society of Chemistry be held responsible for any errors or omissions in this *Accepted Manuscript* or any consequences arising from the use of any information it contains.

**Atmospheric plasma-sprayed $\text{La}_{0.8}\text{Sr}_{0.2}\text{Ga}_{0.8}\text{Mg}_{0.2}\text{O}_3$ electrolyte membranes for
intermediate-temperature solid oxide fuel cells**

*Shan-Lin Zhang,^a Tao Liu^a, Chang-Jiu Li,^a Shu-Wei Yao^a, Cheng-Xin Li,^{*a}*

Guan-Jun Yang,^a Meilin Liu^b

*^a State Key Laboratory for Mechanical Behavior of Materials, School of Materials Science and
Engineering, Xi'an Jiaotong University, Xi'an, Shaanxi, China,*

**E-mail: licx@mail.xjtu.edu.cn*

*^b School of Materials Science and Engineering, Center for Innovative Fuel Cell and Battery
Technologies, Georgia Institute of Technology, 771 Ferst Drive, Atlanta, Georgia, USA.*

Abstract

$\text{La}_{0.8}\text{Sr}_{0.2}\text{Ga}_{0.8}\text{Mg}_{0.2}\text{O}_3$ (LSGM) is considered a promising electrolyte material for intermediate-temperature solid oxide fuel cells (IT-SOFCs) because of its high ionic conductivity. However, a main challenge in the application of LSGM is how to fabricate dense and thin LSGM membranes on electrode substrates at relatively low temperature (it is difficult to sinter LSGM to full density below 1500 °C). In this study, we report our findings in preparation of thin LSGM electrolyte membranes using low-cost atmospheric plasma spraying (APS) process. The phase composition, microstructure, and ionic conductivity of LSGM membranes deposited on anode substrate depend sensitively on the particle size of LSGM powders because Gallium (Ga) may evaporate during the APS process. When the particle size is <30 μm, Ga evaporation increases rapidly with the decrease in particle size, which may dramatically reduce the ionic conductivity of the LSGM deposits. For example, the ionic conductivity of an LSGM deposit was only ~4.2% of the bulk conductivity, even though the deposits may be well bonded (with >80% inter-lamellar bonding ratio), as referred from the thermal

conductivity measurement of the LSGM deposit (>80% of the bulk thermal conductivity). Using LSGM powders with particle sizes >30 μm , we have fabricated LSGM membranes having ionic conductivity of $\sim 0.075 \text{ S cm}^{-1}$ at 800 $^{\circ}\text{C}$, $\sim 78\%$ of the bulk value. Test cells based on plasma sprayed LSGM electrolyte membranes show excellent performance at 600–800 $^{\circ}\text{C}$, suggesting that atmospheric plasma spraying is a promising approach for large-scale manufacturing of high-performance IT-SOFCs.

Key words: SOFC, LSGM, electrolyte, plasma spraying

1. Introduction

Solid oxide fuel cells (SOFCs) have been widely investigated as an efficient and environment-friendly alternative to the conventional power generation using fossil fuels¹⁻⁴. Recently, one of the major concerns on the development of SOFCs is to reduce the operating temperature to less than 700 $^{\circ}\text{C}$ to accelerate the commercialization of SOFC technologies^{5,6}. Since the operating temperature is very sensitive to the ionic conductivity of the electrolyte, a critical step toward intermediate-temperature SOFCs (IT-SOFCs) is the development of an electrolyte of high ionic conductivity⁷⁻¹⁰. To date, $\text{La}_{0.8}\text{Sr}_{0.2}\text{Ga}_{0.8}\text{Mg}_{0.2}\text{O}_3$ (LSGM) is considered a promising electrolyte material for IT-SOFCs at 600–800 $^{\circ}\text{C}$ because of its high ionic conductivity at relatively low temperature and stability over a wide range of oxygen partial pressure^{11,12}. LSGM has an ionic conductivity of $>0.005 \text{ S cm}^{-1}$ at 500 $^{\circ}\text{C}$ ¹³ while a conventional yttria-stabilized zirconia (YSZ) has a similar conductivity at 680 $^{\circ}\text{C}$ ¹⁴. Moreover, LSGM shows excellent chemical compatibility with many perovskite cathode materials used in SOFCs¹.

However, the fabrication of LSGM into a thin, dense membrane faces two challenges: segregation of secondary phases (e.g., LaSrGaO_4 and $\text{LaSrGa}_3\text{O}_7$) during synthesis¹⁵ and a high sintering temperature ($\sim 1500 \text{ }^{\circ}\text{C}$) necessary to obtain sufficient density¹⁶. For example, a solid-state sintering process may

require a sintering temperature as high as 1,500 °C and a sintering time as long as 10 h. Such sintering conditions may lead to abnormal grain growth, dramatically degrading its mechanical properties and structural integrity. Also, it is difficult to prepare a thin electrolyte membrane supported by an electrode (either anode or cathode) because of the potential electrolyte-electrode reactions under the sintering conditions¹⁷⁻¹⁹. As a result, cells based on LSGM electrolyte are usually supported by a thick electrolyte membrane (e.g., ~300 μm), which severely limits the cell performance^{20,21}. Although sintering aids have been used to reduce the sintering temperature down to ~1,300 °C²², the ionic conductivity and the long-time stability may be compromised because of due to the presence of undesirable second phases. To overcome these difficulties, other sophisticated fabrication techniques have also been used. For example, Ishihara et al. reported that a cell assembled with 5 μm thick LSGM electrolyte prepared by pulsed laser deposition (PLD) exhibited a superior performance²³. Sasaki et al. also reported that a dense LSGM electrolyte with a thickness of ~ 1.6 to 5 μm can be prepared by RF magnetron sputtering²⁴. However, for large scale production, the efficiency and cost of these processes could be concern. Thus, it is highly desirable to develop a cost-effective approach for fabrication of dense, thin LSGM membranes on electrode supports without high-temperature sintering.

In recent years, atmospheric plasma spraying (APS) has been developed and used for cost-effective fabrication of SOFC because APS is a proven low-cost, large-scale industrial production process²⁵. Thus, application of APS may greatly accelerate the commercialization of SOFC technology. Both dense electrolyte²⁶⁻²⁸ and porous electrode²⁹⁻³¹ layers can be produced using APS. Dense LSGM electrolyte membranes were also prepared using APS³²⁻³⁴. The unique advantage of APS is that thin electrolyte membranes can be prepared on electrode or metal support without high-temperature sintering. However, the ionic conductivity of the plasma-sprayed LSGM deposits showed large

differences in different studies. Ma et al. reported that the ionic conductivity of plasma-sprayed LSGM films reached $\sim 0.085 \text{ S cm}^{-1}$ at $800 \text{ }^\circ\text{C}$, very close to the conductivity reported for a well-sintered dense bulk sample³³. However, Hwang et al. reported that the plasma-sprayed LSGM deposit showed a conductivity of $\sim 0.054 \text{ S cm}^{-1}$ at $800 \text{ }^\circ\text{C}$ ³², only $\sim 50 \%$ of the value for a sintered bulk sample⁹. In our previous study, the plasma-sprayed dense LSGM deposit exhibited a conductivity of only $\sim 0.008 \text{ S cm}^{-1}$ at $800 \text{ }^\circ\text{C}$ ³⁴. It was noticed that, among these investigations, all LSGMs were deposited with a LSGM feedstock powders of a nominal perovskite crystalline structure and comparable compositions, and all LSGM deposits showed a dense microstructure with little difference in appearance. However, the ionic conductivity of the LSGM deposits varied in a wide range (about one order of magnitude). To date, the fundamental cause has not been reasonably explained for such large variation in ionic conductivities reported by different investigators. It is still not clear what factors control the ionic conductivity of the LSGM deposited through rapid heating of micro-sized particles to molten state by high temperature plasma jet of several thousands of degrees and then rapid splat cooling process. In order to deposit LSGM membranes with consistent ionic conductivity to assemble cells of high performance, it is essential to identify and control the factors that critically impact the ionic conductivity of the plasma-sprayed LSGM electrolyte.

In our recent study, we first found that the evaporation of Ga during the plasma spraying process significantly affected the properties of plasma-sprayed LSGM deposit. We then found that the critical bonding temperature of LSGM was $< 300 \text{ }^\circ\text{C}$, which benefit the application of APS to prepare dense electrolytes. To confirm the controlling factors, a series of experiments and theoretical analysis were performed. First, the effects of LSGM particle size and spray parameters on the microstructure, phase composition, and evaporation were systematically investigated. Then, the behavior of interlamellar

growth of dense electrolyte deposition was studied. Finally, the ionic conductivity and the electrochemical performance of the deposited LSGM membranes was evaluated and correlated with the phase composition and the microscopic features. These studies have helped us to gain insights into the mechanism of membrane deposition and provided us with useful guidelines for preparation of superior LSGM electrolyte membranes by APS.

2. Experimental

2.1 Selection of LSGM powder

Two types of fuse-crushed $\text{La}_{0.8}\text{Sr}_{0.2}\text{Ga}_{0.8}\text{Mg}_{0.2}\text{O}_3$ powders with different particle size distributions (Toshima MFG Co., Ltd., Japan), denoted as powder A and powder B, were used as the source electrolyte powder. Typical morphologies of two types of LSGM powders are shown in Fig. 1. Powder B was obtained from the Powder A by sieving out the small particles from powder A. Therefore, the large particles in both samples have similar shape and morphologies, as seen in Figs. 1 (a) and (b). Fig. 1 (c) shows the size distributions of two powders. It can be seen that the Powder A shows an essential lognormal large distribution with characteristic particle sizes of 6 μm (d_{10}), 25 μm (d_{50}), and 66 μm (d_{90}), while the Powder B shows an essential lognormal distribution with characteristic particle sizes of 20 μm (d_{10}), 56 μm (d_{50}), and 90 μm (d_{90}).

2.2 Spraying process and characterization of the deposits

LSGM was deposited using a commercial plasma spray system (GDP-80, Jiujiang, China). The nozzle of the plasma torch has a diameter of 5.5 mm. Typical spray parameters are listed in Table 1. To study the deposition behavior, single splats were deposited on polished 8 mol% YSZ substrates at different spray distances. The spray distance was measured from the powder injection point to the location

where substrate is placed. To investigate the effect of the deposition temperature on the microstructure, the LSGM electrolytes were deposited at different substrate preheating temperatures. The substrate (combined with support) was heated using a flame torch, and the temperature was monitored using a pyrometer (RAYRPM30L3U, Raytek, USA). The deposits used to measure the electrical and thermal conductivities were deposited on an aluminum substrate with a diameter of 13 mm and a thickness of 1 mm. The free-standing deposits were obtained after the aluminum substrates were dissolved by soaking sprayed samples in a sodium hydroxide solution. Before the characterization, the deposits were annealed at 800 °C in air for 5 h. The phase structures of the deposits were characterized by X-ray diffraction (XRD) analysis (Xpert PRO, PANalytical, Netherlands). Besides, the phase distributions of the deposits were characterized by electron backscattered diffraction (EBSD) analysis (Aztec, Oxford, England). The microstructures of the deposits and splats were examined using scanning electron microscopy (SEM, TESCAN MIRA 3 LMH, Czech) and high-resolution transmission electron microscopy (HR-TEM, JEM-2100F, JEOL). Moreover, the elemental compositions of the deposits and splats were characterized using energy-dispersive X-ray spectroscopy (EDX). The thicknesses of the splats were measured using both three-dimensional (3D) laser confocal scanning microscope and SEM. The ionic conductivities of the LSGM deposits and bulk LSGM samples (sintered at 1550 °C for 10 h) were measured using impedance spectroscopy³⁵ (Solartron SI 1260/1287 impedance analyzer) in the frequency range 0.1 to 100 kHz with an applied AC voltage of 25 mV. The thermal conductivities of the deposits and the bulk sample were measured using a laser flash thermal analyzer (LFA457, NETZSCH, Germany) at the temperature range of 25–1000 °C.

2.3 Numerical analysis of the properties of plasma jet and in-flight particles

To investigate Ga evaporation, the properties of plasma jet and in-flight particles were analyzed by

numerical methods. Because the characteristics of plasma jet outside the torch were determined by the plasma arc and plasma gas inside the torch, the behavior of the plasma gas inside the torch was simulated first. An improved local thermal equilibrium (LTE) model was used to describe the plasma arc. The detailed description of the mathematical model and algorithm process can be found elsewhere^{36,37}. The geometry used in the current study corresponding to the GDP-80 plasma torch is shown in Fig. 2 (a). The throat of the anode nozzle and gas outlet has a diameter of 5.5 and 7.5 mm, respectively. The computational domain formed by the internal region of the torch is limited by the cathode, gas inlet, anode, and gas outlet.

Then, the gas temperature and velocity profiles at the plasma torch exit were employed as the boundary conditions for plasma jet simulations. The plasma jet was simulated by the conventional LTE model³⁸. Because the fluctuations of the plasma jet are caused not only by the arc fluctuations inside the torch, but also by the injection of powder-feeding gas or the involvement of ambient gas, the steady-state plasma arc and jet that are sufficient for guiding the APS process were simulated. As shown in Fig. 2 (b), the computational domain of plasma jet was divided into four faces: gas inlet, nozzle wall, atmospheric boundary, and gas outlet.

Finally, the particle behavior in the plasma jet was simulated. The particles were injected at a distance of 10 mm from the torch exit with an initial radial velocity of 15 m s^{-1} . To simplify the calculations, the particles were assumed to be spherical. The spherical particle is heated up (or cooled down) by surrounding plasma gas by heat convection and thermal radiation. The temperature distribution within the particle is then governed by heat conduction, which can be found elsewhere³⁹. After the particle temperature, velocity, and radial position at the torch exit were obtained, these parameters were employed as the initial conditions of the simulations in plasma jet. Table 2 shows the properties of the

LSGM particles utilized in simulation. All the models were solved by FLUENT, a commercial computational fluid dynamics (CFD) software developed by Ansys Inc. Besides, in order to verify the simulation results, the in-flight particle temperature and velocity were measured by DPV-2000 system (Saint-Bruno, QC, Canada).

2.4 Fabrication and characterization of SOFC single cells

The SOFC single cells were supported by a NiO/YSZ anode support. The NiO/YSZ supports with a diameter of 22 mm and a thickness of 0.4 mm were prepared by the tape-casting method. In order to prevent the reaction of Ni anode with LSGM electrolyte⁴⁰, Gadolinium-doped ceria (GDC) interlayer with a thickness of 2–3 μm was prepared on the anode by tape casting. The LSGM electrolyte was deposited at a spray distance of 80 mm. The thickness of electrolyte was controlled at a range of 50–55 μm . Finally, $\text{La}_{0.6}\text{Sr}_{0.4}\text{Co}_{0.2}\text{Fe}_{0.8}\text{O}_3$ (LSCF) cathodes were deposited on the electrolyte with an area of 0.8 cm^2 and a thickness of 20–30 μm . Commercially available agglomerated LSCF powders (Sulzer-Metco, USA) with a size range of 20–50 μm was used. The plasma spray parameters for electrolyte and cathode are listed in Table 1.

Before the performance testing, the cell was annealed at 800 $^{\circ}\text{C}$ in air for 5 h. The performance of the single cell was tested in a furnace with a heating and cooling rate of 3 $^{\circ}\text{C min}^{-1}$. H_2 fuel was bubbled through water maintained at ~ 30 $^{\circ}\text{C}$. After the anode was reduced in H_2 at 800 $^{\circ}\text{C}$ for 2 h, the output performance of the cell (I - V and I - P curves) was measured in the temperature range 600–800 $^{\circ}\text{C}$ under a H_2 flow of 0.05 slpm and an air flow of 0.15 slpm. The electrochemical properties of the cell were measured using impedance spectroscopy in the frequency range 0.1–100 kHz with an applied AC voltage of 25 mV.

3. Results and discussion

3.1 Deposition behavior of LSGM single splats

We first deposited single splats on polished YSZ substrates with a deposition temperature of ~ 350 °C to study the deposition behavior. Fig. 3 shows the surface morphologies of the splats deposited at a spray distance of 90 mm. Clearly, the individual splats exhibited a regular disk shape because the desorption of the possible adsorbents from the substrate surface occurred prior to the impinging of droplet when the substrate was preheated to the above mentioned deposition temperature. Moreover, the splats showed a smooth surface with no cracks, attributed to the high deposition temperature and beneficial to the formation of a dense electrolyte membrane.

The elemental compositions of the plasma-sprayed LSGM splats were determined using EDX. While the contents of La, Sr, and Mg in a splat were very close to those of the starting powder, Ga was found to evaporate during the spraying process. In order to study quantify the loss of Ga due to evaporation, the content of La was used as the reference because of its low vapor pressure^{41,42}.

Fig. 4 (a) shows the effects of splat diameter and spray distance on the molar ratio of Ga to La. It was found that the molar ratio of Ga to La is varied from 1 in the starting powder to a value less than 0.1, depending on the splat diameter and spray distance. At a spray distance of 30 mm, the molar ratios of Ga to La for all splats with different particle sizes were very close to 1.0, indicating that the Ga evaporation can be ignored. When the spray distance was increased to 50 mm, the molar ratio of Ga to La was reduced to ~ 0.68 in the splats with a diameter of ~ 15 μm . However, it was found that the molar ratio increased with the increase of the splat diameter, approaching ~ 1.0 when the splat diameter was increased to ~ 80 μm . The molar ratio remained unchanged when splat diameter was further increased. Moreover, when the spray distance was increased to 70, 90, and 110 mm, the molar ratio of Ga to La

was reduced to ~ 0.1 for the splats of 10–15 μm in diameter, indicating that almost 90% of Ga evaporated during the spraying process. Moreover, the molar ratio also increased to 1.0 when the splat diameter increased to over 80 μm at these spray distances.

Through the measurement of the diameter, thickness and volume for each splat using 3D confocal laser scanning microscopy, the apparent diameter of molten spray particle prior to deposition can be calculated for each splat supposing that spray particles are in a spherical shape. Thereafter, the relationship between the Ga/La ratio and the splat diameter can be converted to the relationship between the Ga/La ratio and spray particle diameter under individual spray conditions. Supposing that the evaporation loss of La element can be neglected, the Ga/La ratio of each splat reflects the Ga evaporation loss during in-flight of the spray particle with plasma jet. Fig.4 (b) shows the effects of particle size and spray distance on Ga evaporation loss. The molar ratio of Ga in the starting powder is equal to that of La. Based on the results shown in Fig. 4 (b), it is clear that spray particle size influences significantly the Ga evaporation loss during plasma spraying of LSGM. When the particle diameter is larger than 30 μm , the Ga evaporation can be neglected at whole in-flight process. When the particle diameter is less than 30 μm , Ga evaporation of a spray particle takes place in three distinct spray distance regions with spray particle travelling in the plasma jet. When the spray distance is less than 30 mm (stage I), no evaporation was observed for all the particles. However, when the spray distance increased from 30 mm to 70 mm (stage II), the Ga evaporation loss increased with the increase of the spray distance. Moreover, no further Ga evaporation loss was observed when the spray distance became larger than 70 mm (stage III). Moreover, the evaporation loss increased with the decrease of the particle size when the particle diameter is less than 30 μm . Therefore, it is clear that the Ga evaporation of LSGM spray particles during plasma spraying mainly occurs during in-flight from 30

mm to 70 mm for the particles of a diameter less than 30 μm .

3.2 Numerical analysis of the properties of plasma gas and in-flight particles

To gain some insight into the evaporation phenomenon, which is determined mainly by particle temperature and its dwelling time within the high-temperature region of plasma jet, the in-flight particle parameters were studied using numerical simulation. The particles are injected into the plasma jet at a distance of 10 mm away from the exit of the torch nozzle. The parameters of spray particles are determined by the interaction of spray particle with plasma jet, which is in turn determined by the properties of plasma gas inside the torch. Therefore, we first examined the properties of plasma gas inside the torch and the plasma jet by numerical analysis. Shown in Figs. 5 (a) and (b), respectively, are the simulated gas temperature and velocity distribution inside the torch under the parameters listed in Table 1 for electrolyte deposition. The gas temperature and velocity distributions are almost axisymmetrical inside the torch. The plasma core temperature is $\sim 34,000$ K. The maximum velocity inside the torch is $\sim 2,100$ m s^{-1} at the throat because of the expansion of the nozzle. The gas temperature and velocity distribution at the torch exit were used as the gas inlet boundary conditions for the simulations of plasma jet. The calculated gas temperature and velocity distributions of the plasma jet are shown in Figs. 5 (c) and (d), respectively. The gas temperature and velocity decrease rapidly with the increase of the axial distance. The simulated gas temperature and velocity of plasma jet and inside the torch are close to those reported in the literature³⁶⁻³⁸.

The simulated temperature and velocity for in-flight particles of different diameters are shown in Fig. 6. The particle velocity increases with the increase of the spray distance up to 50 mm and then decrease with the further increase in the spray distance. Moreover, the maximum particle velocity increases with the decrease in particle size. Besides, from the particles surface temperature, it can be analysed that

when it reached melting point (1,700 °C) the melting process begins, and the particle completely melts when the core temperature exceeded the melting point. As can be seen from Fig. 6 (b), particle with the size of 10 μm begins to melt at the spray distance of 8 mm and entirely melts at 21 mm (From Fig. 6 (c)). Even the particle with the size of 50 μm begins to melt at 28 mm, however, the particle diameter is large hence its core doesn't melt at 100 mm. According to the melting process, the melting degree (volume fraction of liquid phase) for in-flight particles of different diameters is shown in Fig. 6 (d). Moreover, both the maximum particle surface temperature and core temperature increase with the decrease in particle size. When the particle diameter is larger than 30 μm, its temperature is lower than 2,500 °C. However, for the powder with a particle size of 10 μm in diameter, the particle surface temperature reaches >3,500 °C, which is much higher than the melting point of LSGM.

3.3 Process and mechanism of Ga evaporation

Based on the numerical analysis, the Ga evaporation mechanisms can be proposed to explain the effect of particle size and spray distance on the melt flow within spray particle using the spherical Hill vortex model^{43,44}, which predicts that significant convective movement of molten melt takes place within the droplet (a fully molten particle). As shown in Fig. 4, two mechanisms are responsible for Ga evaporation during in-flight of LSGM spray particle. As can be seen from Fig. 6 (d), when a LSGM particle is injected into plasma jet, it is heated to molten state gradually from particle surface and thus the thickness of molten layer gradually increases. The reported results indicate that the evaporation rate of Ga in LSGM almost increases exponentially with the increase of temperature^{41,42}. Since Ga evaporates much fast at a temperature over the melting point of LSGM⁴¹, Ga evaporates from the surface rapidly, resulting in a shell with less Ga and the Ga evaporation will then be controlled by the outward diffusion of Ga element from the inner of the droplet. As schematically shown in Fig. 7, spray

particles in stage I are rapidly heated to the highest surface temperature based on the evolution of particle temperature shown in Fig. 6 (b), leading to remarkable Ga evaporation. It may be expected that the Ga evaporation occurs remarkably. However, it is clear, as shown as in Fig. 4, that Ga evaporation was then limited by the mass transport through the Ga-deficient surface layer, due to limited diffusion time with high velocity in-flight particles. Thus, a stable Ga-deficient surface layer forms a barrier to protect LSGM spray particle from further loss of Ga.

On the other hand, when the spray particle is fully molten, the Hill vortex convection through molten droplet takes place in the case that the Reynolds number ($Re = \rho D |V_g - V_p| / \mu$, where ρ , V_g , V_p , D , and μ are the density, gas velocity, particle velocity, particle diameter, and viscosity, respectively) of the droplet is large enough, which is resulted from the difference of kinematic viscosities between the liquid droplets and surrounding media⁴⁴. For particles with a size $< 30 \mu\text{m}$, the full molten state can be reached at the spray distance of $\sim 30 \text{ mm}$, as predicted by the simulation results (Fig. 6 (d)). Rapid Ga evaporation from the surface results in a Ga-deficient shell. However, the generated vortex continuously destroys the shell, being a diffusion kinetic dominant layer, through turbulent mixing of melt within liquid splat. As a result, rapid mass transport of Ga element within the whole molten particle occurs by vortex flow, leading to rapid redistribution of Ga uniformly throughout the bulk volume of the droplet. With the disappearance of the shell, the fresh liquid phase with a high Ga content was exposed on the particle surface and evaporated continually. The intensity of the convective movements was almost proportional to the Reynolds number. The simulation results indicate that the particle temperature, which significantly affects the viscosity, decreased with a decrease in particle size. In general, the viscosity of a droplet is proportional to temperature. Therefore, the intensity of the convective movements of the smaller particles was much higher than that of the larger particles. For the

particle with a size of 30 μm , the evaporation begins to increase at the spray distance of 50 mm (Fig. 4). This is because the particles reach full molten state at ~ 50 mm (Fig. 6 (d)) and the vortex flow effect starts at this spray distance. When the particle diameters are more than 30 μm , the intensity of the convective movement could be ignored. This is because when large particles reach full molten state, its velocity difference from that of plasma jet becomes much less and the vortex flow effect becomes negligible. Therefore, the evaporation of LSGM particle depends on the effect of vortex flow during in-flight state. Since the smaller particles reach the full molten state fast with a larger velocity difference from plasma jet, Ga loss of the smaller particles is much higher greater than that of the larger particles.

Moreover, this model can also be used to explain the effect of spray distance on evaporation. Fig. 8 shows the comparison of simulated particle surface temperature and velocity for the 10 μm particles with that measured by DPV-2000. It was obviously found that the particle temperature and velocity measured by DPV-2000 agreed well with the simulation results. In stage I, the Ga evaporation can be neglected since the low temperature and limited diffusion time. As discussed above, in stage II, the evaporation increased with the increase of spray distance, showing a linear relationship. This can be attributed to the convective movements as confirmed above. On the one hand, as shown in Fig. 8 (a), the 10 μm particle in stage II has a high temperature more than 3,000 $^{\circ}\text{C}$. On the other hand, there is a big velocity difference between the spray particle and plasma gas around it (Fig. 8 (b)), implying that there is strong convection inside the full molten particle. However, for a spray distance of >70 mm (stage III), the evaporation changed slightly with the increase in the spray distance. On one hand, the particle temperature decreased rapidly when the spray distance was >70 mm. Thus, the evaporation rate decreased with the decrease in temperature. On the other hand, when the spray distance exceeded 70

mm, the particles flew out of the jet core. As shown in Fig. 8 (b), the velocities and temperatures of the plasma jet and particles converged, thus decreasing the Reynolds number rapidly. As the kinematic viscosity decreased rapidly, the convective movement stopped. Therefore, at distances further than 70 mm, the dominating mechanism of evaporation is the element diffusion, which is a very slow process. Therefore, the evaporation changed slightly with the increase in the spray distance when it was >70 mm. Thus, the evaporation mainly occurred within the first 30–70 mm downstream of the nozzle exit.

As shown in Fig. 7, two types of evaporated particles may be present after the evaporation. One of the particles fully remixed during the convection process; thus, the particle showed a uniform composition (particle I). However, there was another type of particle (particle II) where a stable shell was maintained or another evaporated shell was formed after the convection process. For this particle, the composition is not uniform. The Ga content in the shell was much lower than that inside the particle. This type particle with a thin Ga-deficient shell may also be found from the particles with a size more than 30 μm because of the rapidly evaporation from the surface. Besides, the third type was the particle without Ga evaporation from the big spray particle.

Figure 9 shows the microstructure of the fractured LSGM splats. First, the splats showed a thickness of $\sim 0.8\text{--}1.2\ \mu\text{m}$ and bonded well with the substrate. Then, three types of splats as mentioned above were found. The first type of splat with rough fractured surface which contain many small grains (50–100 nm) is shown in Fig. 9 (a). EDX analysis showed that almost all the Ga evaporated in this type particle. Another type is shown in Fig. 9 (b). In this type, the Ga-deficient shell with a thickness of $\sim 300\ \text{nm}$ was observed at the lower portion of the splat. As indicated by the arrows, this region also contains small grains. Moreover, EDX analysis showed that Ga in the evaporated shell was much lower than other region. The third type of splat without Ga evaporation is shown in Fig. 9 (c). It was found that

this type splat presents a smooth and homogeneous fractured surface.

3.4 Behavior of interlamellar bonding formation

The microstructure of plasma-sprayed ceramic coatings depends not only on the particle size, particle temperature, and particle velocity, but also on the deposition temperature²⁶. As shown in Fig. 10, the LSGM electrolyte deposited without preheating the substrate (<150 °C) produced a typical lamellar structure. The non-bonded interfaces and intra-splat cracks (as indicated by arrows) are clearly present in the deposit, consulting a porosity of $\sim 5.5 \pm 0.5\%$. Thus, the plasma-sprayed LSGM following the conventional routine is not suitable for high performance SOFC electrolytes because of low conductivity and poor gas tightness.

However, as shown in Fig. 11, when the substrate was preheated to a temperature higher than 300 °C, the non-bonded interfaces and intra-splat cracks in the deposit disappeared. The deposited LSGM had a dense microstructure with well bonded lamellae, and the porosity was reduced to $\sim 2.3 \pm 0.7\%$. The increase of the lamellar bonding ratio and decrease of intra-splat cracks and porosity improve the electrolyte conductivity and gas tightness.

Our previous investigation²⁶ showed that when the deposition temperature is higher than 680 °C, the microstructure of YSZ coatings deposited by APS changes from the typical lamellar structure with limited lamellar bonding to the continuous columnar crystal structure. Moreover, for plasma-sprayed Al₂O₃ coatings⁴⁵, the mean interface bonding ratio increased significantly when the deposition temperature was higher than 500 °C. The recent investigations reveal that there is a critical deposition temperature for spray molten droplet to bond completely to the previously deposited splats^{46,47}, which is referred to as the critical bonding temperature. The present study indicated that the critical bonding

temperature of LSGM was lower than 300 °C, which is far lower than that of YSZ because the melting point of LSGM (~1,700 °C) is much lower than that of YSZ (~2,700 °C). Therefore, it is the low critical bonding temperature of LSGM that benefits the application of APS to prepare dense electrolytes.

3.5 Effect of Ga evaporation on the microstructure and phase structure

3.5.1 Microstructure

Fig. 12 (a) shows the cross-sectional microstructure of the as-deposited LSGM using powder A, which contained many small particles less than 30 μm in diameter. A close examination revealed the existence of some white-striped regions with a thickness of ~0.5–1 μm, as shown in the inset in Fig. 12 (a). The EDX line scans of La, Sr, Ga, and Mg elements across this region are shown in Fig. 12 (b). The results indicate that these regions have less Ga and relatively more La. Therefore, it is clear that these Ga deficient regions were formed by the droplets which experienced significant Ga evaporation. Those regions are present on the fractured cross-section as shown in Fig. 12 (c). It is evident that the Ga deficient regions contain small grains with a size of 50–100 nm, which can be recognized from the splat shown in the inset of Fig. 12 (c). Moreover, the Ga deficient regions were also recognized on the fractured surface of the annealed deposits (Fig. 12 (d)).

Figure 13 (a) shows the TEM bright-field image of a cross-section of the as-sprayed LSGM electrolyte. The EDX mappings (Fig. 13 (b)) show that the striped region (with a thickness of ~300 nm) has less Ga, corresponding to the above mentioned Ga-deficient region. The diffused halo rings in the selected area electron diffraction (SAD) patterns indicate that both sides of the Ga-deficient region contain an amorphous phase (as marked by C in Fig. 13 (a)). The formation of an amorphous phase can be

attributed to the rapid solidification process inherent to thermal spray process, as observed in other investigations³²⁻³⁴. Moreover, the SAD patterns revealed that the Ga-deficient region has a cubic perovskite structure; even though this region is poor in Ga. However, as shown in Fig. 13 (c), the electron diffraction image of the Ga-deficient region (marked as A in Fig. 13 (a)) revealed many defects such as missing atoms and irregular arrangements in this region because of Ga deficiency. Moreover, the HR-TEM image (Fig. 13 (d)) of the region marked as B in Fig. 13 (a) shows that the interface between the Ga-evaporated and non-evaporated regions has a chemical bonding.

To compare the structural differences between the Ga-deficient and Ga-rich regions, we examined the crystal structure of the region without Ga evaporation in the deposit using HR-TEM, as shown in Fig. 14 (a). The EDX analysis showed that Ga evaporation is negligible in this region. The SAD patterns indicate that this region has a cubic perovskite structure with high crystallinity. Fig. 14 (b) shows the electron diffraction image of the region marked as A in Fig. 14 (a). The atoms in this region were neatly arranged, and crystal lattice disfigurement was not observed. Therefore, it can be concluded that the Ga evaporation slightly affected the crystal; however, crystal lattice disfigurement occurred during the droplet solidification process.

Our results suggest that the plasma-sprayed LSGM deposits with negligible Ga evaporation can be achieved using LSGM powders with a particle size of $>30\ \mu\text{m}$. Indeed, when powder B, which has few fine powders ($<30\ \mu\text{m}$), was used to deposit the LSGM electrolyte, the results were much better. Figs 15 (a) and (b) show the microstructures of a polished and fractured cross-section of the LSGM deposit prepared from powder B, respectively. The polished cross-section shows that the deposit has a dense microstructure, with few closed pores. Moreover, a few of semi-molten particles were present in the deposit because the large-size particles did not melt completely.

However, a good interface bonding was observed between the completely molten and semi-molten particles. Moreover, as predicted, the white-striped regions were not found in the deposit, indicating that Ga evaporation was insignificant in the spraying process. Fig. 15 (b) shows the cross-section of the deposit; this result also reveals that the interfaces of the splats deposited by fully molten or semi-molten particles were bonded well together. Furthermore, apparent Ga-deficient regions were also absent in the fractured cross-section of the deposit.

3.5.2 Phase structure

Figure 16 (a) shows the XRD patterns of the LSGM deposits prepared from powder A. First, the original powders exhibited a single phase of perovskite structure similar to the standard XRD pattern of undoped LaGaO_3 (PDF 24-1102), and no other impure phase was observed. Second, the as-sprayed deposit contained large amounts of amorphous phase identified by a broad peak with the maximum intensity at a 2θ angle of $\sim 32^\circ$. Previous studies reported that the recrystallization temperature of the amorphous phase in the as-sprayed LSGM deposit was $\sim 800^\circ\text{C}$ ³²⁻³⁴. Therefore, the deposit was annealed at 800°C in air for 5 h. After the annealing, the LSGM deposit had a high degree of crystallization, and the broad peak of amorphous phase disappeared. However, a slight amount of new phase, LaSrGaO_4 , was observed in the annealed deposit. Fig. 16 (b) shows the phase structure of the LSGM electrolyte prepared from powder B. Clearly, it has a single-phase perovskite structure. Moreover, the amorphous phase was also present in the as-sprayed deposit, similar to the deposit prepared from powder A. However, the annealed deposit showed a single phase without the impurity phases observed in the annealed deposit from powder A. Therefore, it can be concluded that the formation of LaSrGaO_4 in the annealing process can be attributed to Ga evaporation, resulting in a metastable structure in these Ga-deficient regions.

Figure 17 shows the cross-sectional crystal orientation and phase distribution map obtained by EBSD analysis for the annealed LSGM deposit prepared from powder A. Different colors of the microstructures and grain boundaries shown in Fig. 17 (a) represent different grain growth orientations. Different color grain boundaries shown in Fig. 17 (b) represent different phases. Both the orientation and phase distribution maps showed a lamellar structure because the deposition was carried out by a layer-by-layer manner. The orientation map indicated that the grains of the deposit have no preferred orientations. The phase distribution map revealed that the deposit contains LSGM and LaSrGaO₄, being consistent with the XRD analysis. Moreover, most of the LaSrGaO₄ showed a lamellar structure and smaller grains than the LSGM phase. Wioletta K-K et al.⁴¹ also reported that the impurity phase of LaSrGaO₄ was observed in the samples after vaporization measurements. LaSrGaO₄ shows a tetragonal structure (PDF 24-1208) with a very low conductivity. LaSrGaO₄ usually appeared in the LSGM powder preparation¹³ and electrolyte sintering processes⁴⁸, the evolution of which results in significant performance degradation of the resultant cell.

3.6 Microstructural development of plasma sprayed LSGM

3.6.1 Microstructural evolutions

The main purpose of this study was to prepare an LSGM electrolyte with dense microstructure and high conductivity by APS. The essential issue is how to design and optimize the structure of a deposit. Based on the results mentioned above, strategically, it can be achieved by optimizing the parameters and powders. Fig. 18 shows the schematic diagram of the microstructural developments of plasma-spraying of LSGM electrolyte by different route. Fig. 18 (a) shows the plasma spraying of LSGM electrolyte by the LSGM powder with a wide range of particle size distribution, especially

containing substantial amount of small particles, and without deposition temperature control (i.e., preheating). Many defects are present in LSGM deposits. First, the mean bonding ratio was only ~30–35% because the deposit grows with a lamellar structure. Moreover, a low deposition temperature results in many intra-splat cracks and closed pores (6–8%). As mentioned above, significant Ga evaporation from small particles will lead to the formation of nonstoichiometric regions and impurity phase. Fig. 18 (b) shows the schematic microstructure of LSGM deposited with a wide range of particle size distribution but with deposition temperature control. According to the discussion in section 3.2, the lamellar bonding ratio of the deposit increases significantly due to the higher deposition temperature than the critical one (Fig. 18 (b)). Moreover, the intra-splat cracks disappear, and the porosity decreases to a low level. However, the secondary phase of LaSrGaO_4 resulting from the Ga-deficient particles, which experience significant Ga evaporation loss due to small particle size, is included in the dense deposit. Since based on the Ga evaporation mechanism, the inclusion of the secondary phase of LaSrGaO_4 can be avoided using the LSGM powders of larger size, Fig. 18 (c) shows schematically the optimized microstructure of the LSGM electrolyte developed by controlling powder particle size and deposition temperature. Thus, the LSGM electrolyte contains no LaSrGaO_4 phase by limiting Ga evaporation and well bonded lamellae, although a few of non-bonded interfaces and closed pores are present in the electrolyte, which are inevitable in a spraying process.

3.6.2 Thermal conductivity of plasma-sprayed LSGM deposit

To compare the properties of the deposits to those of the bulk, dense LSGM bulk samples were prepared. Fig. 19 (a) shows the morphology of a fractured cross-section of the well-sintered LSGM bulk sample, which has a dense structure with large-size grains because of the high sintering temperature and long sintering time. Fig. 19 (b) shows the thermal conductivity of the LSGM bulk

sample and the APS deposits at different temperatures. Clearly, the thermal conductivity increased with the increase of the test temperature. For the sintered bulk sample, the thermal conductivity is $\sim 1.5 \text{ W m}^{-1} \text{ K}^{-1}$ at room temperature and $\sim 2.1 \text{ W m}^{-1} \text{ K}^{-1}$ at $1,000 \text{ }^\circ\text{C}$. The thermal conductivities of the APS deposits prepared from powders A and B are ~ 1.25 and $\sim 1.24 \text{ W m}^{-1} \text{ K}^{-1}$, respectively, at room temperature and increased to ~ 1.68 and $\sim 1.76 \text{ W m}^{-1} \text{ K}^{-1}$ at $1,000 \text{ }^\circ\text{C}$, respectively. The thermal conductivities of the APS deposits prepared from powders A and B are very close, and are higher than 80% of the bulk value. For thermal-sprayed ceramic coatings, the microstructure of the deposit significantly affects its thermal conductivity. Previous studies have shown that the limited bonding at the lamellar interfaces in ceramic coatings reduces thermal conductivity. For example, the thermal conductivity of conventional plasma-sprayed Al_2O_3 coatings was only $\sim 10\%$ of the bulk value⁴⁵ because of the limited lamellar interface bonding ratio. Therefore, thermal conductivity can reflect the interface bonding ratio of the deposits. The present results revealed that the thermal conductivities of the deposits prepared from powders A and B reached $>80\%$ of the bulk, suggesting that the mean interface bonding ratio of the deposits reached $>80\%$. The lamellar interface bonding ratio is significantly affected by the deposition temperature. In our previous study, the mean bonding ratio of the YSZ coatings deposited at room temperature was less than $\sim 32\%$ ⁴⁹. However, it reached $\sim 75\%$ when the deposition temperature was increased to $1,100 \text{ }^\circ\text{C}$ ⁴⁹. The effect of deposition temperature on the interface bonding ratio is different for different materials since the critical deposition temperature for bonding temperature depends on coating material^{46,47}. When the deposition temperature is higher than the critical bonding temperature, the lamellar interface bonding ratio is significantly increased with the increase of the deposition temperature^{46,47}. For Al_2O_3 coatings which has a lower critical bonding temperature of about $300 \text{ }^\circ\text{C}$, the mean lamellar interface bonding ratio increased from 32% to

59% when the deposition temperature was increased from near-room temperature to 660 °C⁴⁵. Since the LSGM deposits were prepared at a deposition temperature of ~300–350 °C, being higher than the critical deposition temperature, they have high interface bonding ratio.

3.7 Ionic conductivity of plasma sprayed LSGM

With a dense microstructure and high lamellar interface bonding ratio, the APS LSGM deposits may have a high ionic conductivity. Figures 20 (a), (b) and (c) show the electrochemical impedance spectra for the LSGM bulk, deposit prepared by powder A and deposit prepared by powder B at different temperatures, respectively. The deposits and sintered bulk samples exhibited different polarization resistance since the difference of microstructure. However, the grain interior and grain boundary contributions on the conductivity cannot be studied separately because electrode processes are dominant in the investigated frequency range and only total conductivity was obtained. Shown in Fig. 21 (a) are the total ionic conductivities of the LSGM deposits and the bulk samples measured at different temperatures. The sintered bulk sample showed an ionic conductivity of ~0.096 S cm⁻¹ at 800 °C, consistent with the data reported in the literature⁴⁸. However, significant difference in the ionic conductivity between the two types of APS deposits was observed, even though the deposits had a similar interface bonding ratio and similar thermal conductivity. For example, at 800 °C, the ionic conductivity of the deposit prepared from powder A was 0.004 S cm⁻¹, which is only 4.2% of the bulk conductivity in this study. However, the ionic conductivity of the deposit prepared from powder B reached 0.075 S cm⁻¹, which is ~78% of the bulk conductivity. The Arrhenius plots of the ionic conductivity for the LSGM bulk samples and the APS deposits are shown in Fig. 21 (b). The activation energy (E_a) for the LSGM bulk sample is ~1.02 eV, being consistent with the data in the literature⁴⁸. The deposit prepared from the powder B has an E_a of ~1.04 eV, which is very close to the E_a of the

bulk sample. However, the E_a of the deposit prepared from the powder A is ~ 0.97 eV, which is slightly less than that of the bulk sample.

Usually, the conductivity of LSGM depends on the composition, the presence of secondary phases, and ceramic microstructure. The large difference in the ionic conductivity between the two types of APS deposits can be explained by the difference in the microstructure and elemental composition. For the annealed LSGM deposit prepared from the powder A, some lamellar LaSrGaO_4 was observed, which is a low conducting material compared to LSGM; also, Ga-deficient splats are present in the deposit (being perpendicular to the direction of oxygen-ion transport), leading to lower ionic conductivity. For plasma-sprayed LSGM electrolyte membrane, oxygen ion transport through the electrolyte deposits is in a direction perpendicular to the lamellae in the deposit. The existence of very low conductivity regions with a lamellar structure and non-bonded interfaces would cut off many of the direct ion transport pathways. Therefore, the ionic conductivity of the deposit would decrease significantly due to the reduction of the effective conduction area and pathways. Moreover, small closed pores would also decrease the effective conduction area. However, the effects of closed pores on the conductivity are insignificant because the pores are small and the porosity is small. In the same manner, as shown in Fig. 18 (c), only some closed pores and non-bonded interfaces were observed in the deposit prepared from the powder B. At 800°C , a conductivity of 0.075 S cm^{-1} was obtained, which is $\sim 78\%$ of the bulk conductivity. The ratios of ionic and thermal conductivities of the deposits to those of the corresponding bulk sample are very close, suggesting that the ionic conductivity of the deposit prepared from the powder B is affected mainly by the non-bonded interfaces and closed pores.

Table 3 summarizes the conductivities of the LSGM electrolytes prepared by APS and solid-phase sintering (SPS) as reported in literature. Clearly, the LSGM electrolytes prepared by APS with different

powders and different parameters showed a large difference in conductivity. As mentioned above, the powder size significantly affected the conductivity because of Ga evaporation, which was clarified in this study. Moreover, the conductivity of the LSGM electrolyte prepared by SPS also showed a large difference in different studies because of the difference in the starting powders and sintering processes. The conductivity of the optimized LSGM electrolyte in this study reached 0.075 S cm^{-1} at $800 \text{ }^\circ\text{C}$ and exceeded the values of the SPS LSGMs reported^{48,50,51}, indicating the promising potential of APS in fabrication of LSGM electrolyte membrane.

3.8 Electrochemical performance of the test cells

Figure 22 (a) shows a cross-sectional view of a SOFC single cell supported by a NiO/YSZ anode. The GDC interlayer on the anode has a thickness of $\sim 2\text{--}3 \text{ }\mu\text{m}$. The two types of LSGM electrolyte membranes deposited on the GDC have a thickness of $\sim 50\text{--}55 \text{ }\mu\text{m}$. The electrolytes adhered well to the GDC. The thickness of the LSCF cathodes deposited on the electrolyte are $\sim 20\text{--}30 \text{ }\mu\text{m}$. The two types of cells with electrolyte membranes prepared from both the powder A and B are referred to as cell A and B, respectively. Fig. 22 (b) shows the microstructure of plasma-sprayed LSCF cathode and the interface of LSGM/LSCF. The plasma-sprayed LSCF cathode showed a porous structure because most LSCF particles were in the semi-molten state during spraying. Moreover, the cathode was bonded well with the electrolyte. Therefore, a well bonded interface and the porous cathode with fine particles would provide more three-phase boundaries (TPBs) for cathode reaction.

The power outputs of the cells are shown in Fig. 23. The cells showed open-circuit voltages (OCV) of $\sim 1.1 \text{ V}$ at $800 \text{ }^\circ\text{C}$. This value is close to the theoretical voltage, indicating that the plasma-sprayed LSGM electrolytes are dense enough. At an operating temperature of $600 \text{ }^\circ\text{C}$, the cell A (Fig. 23 (a))

showed a peak power density of only 13 mW cm^{-2} . When the operating temperature was increased to 650, 700, 750, and 800 °C, the peak power densities of the cell increased to 19, 35, 60, and 95 mW cm^{-2} , respectively. However, when the cell was assembled using the optimized electrolyte membrane through microstructure development, the cell performance enhanced significantly (Fig. 23 (b)). At 600 °C, the cell B showed a peak power density of 85 mW cm^{-2} , which is much higher than that of the cell A. When the cell B was operated at 650, 700, 750, and 800 °C, the peak power densities reached 160, 290, 502, and 712 mW cm^{-2} , respectively. At 800 °C, the power density of the cell B was 7.5 times higher than that of the cell A.

Fig. 23 (c) shows the impedance spectra of the cells obtained at 800 °C under the OCV conditions. The ohmic resistance can be estimated from these spectra from the intercepts with the abscissa at high frequencies. The electrode polarization losses can be obtained from the difference in intercepts with abscissa at low and high frequencies. At 800 °C, the ohmic resistances for cells A and B were 1.4 and $0.1 \Omega \text{ cm}^2$, respectively. Because the electrical conductivity of the anode and cathode are a few orders of magnitude higher than that of the electrolyte, the ohmic losses arise mainly from the LSGM electrolyte and GDC interlayer. The GDC interlayer only had a thickness of 2–3 μm , these values are consistent with the ohmic resistance of 55- μm thickness LSGM electrolytes used in this study. The large difference in the ohmic resistance for the two types of cells can be attributed to the difference in the conductivity of plasma-sprayed LSGM electrolytes. However, a significant difference in the electrode polarization (non-ohmic resistance) of the cells was also observed, even when the cells were assembled with the same anode and cathode. At 800 °C, the electrode polarization for cells A and cell B were 1.6 and $0.3 \Omega \text{ cm}^2$, respectively, which is a combination of anode and cathode impedances. Because the composite anodes were adhered on the GDC interlayer, the anodes for the two types of

cells should be similar. However, the LSCF cathodes were adhered on different LSGM electrolyte membranes. Therefore, the difference between the electrode polarizations may be attributed mainly to the difference in TPBs of the cathodes. The TPBs of the cathode were composed by LSGM, LSCF, and oxygen gas. As shown in Fig. 24 (a), the electrolyte prepared from powder A had an impurity phase of LaSrGaO_4 and the Ga-deficient regions showed very low ionic conductivity. Because of the existence of these regions, the effective surface area of electrolyte decreased, thus subsequently decrease the activity of the TPBs. However, the less conductive phases did not exist in the optimized electrolyte, which would provide more TPBs for the cathode reaction (Fig. 24 (b)). Therefore, the cathodic polarization resistance of the cell A was much higher than that of the cell B.

Hwang et al. reported that the LSGM electrolyte prepared by APS showed a conductivity of $\sim 0.05 \text{ S cm}^{-1}$ at $800 \text{ }^\circ\text{C}$ ³². The LSGM powder had a d_{50} particle size of $\sim 37 \text{ }\mu\text{m}$, which was larger than that of the powder A and smaller than that of the powder B used in this study. Therefore, Ga evaporation maybe occurred in the smaller particles during the spraying process. That is why the ionic conductivity is lower than that obtained in the present study for the deposit prepared by powder B. In their study, the cell assembled with Ni/YSZ anode, plasma-sprayed LSGM electrolyte ($50\text{--}60 \text{ }\mu\text{m}$), and LSCF cathode ($20\text{--}30 \text{ }\mu\text{m}$), which was similar to our study, showed a peak power density of $\sim 440 \text{ mW cm}^{-2}$ at $800 \text{ }^\circ\text{C}$ (H_2 and O_2 were used as the fuel and oxygen gases, respectively). Taking into account of the test condition by H_2/air in the present study, this value reported earlier is much lower than that obtained in the present study for the cell B due possibly to the lower conductivity of electrolyte. Ma et al. also studied the performance of plasma-sprayed LSGM electrolyte. In their study, LSGM powder with a size distribution of $d_{50} \sim 40 \text{ }\mu\text{m}$ was used. The plasma-sprayed LSGM electrolyte showed a conductivity of $\sim 0.085 \text{ S cm}^{-1}$ at $800 \text{ }^\circ\text{C}$ ³³. Even though the electrolyte showed a superior conductivity, the cell

assembled with Ni/YSZ anode, LSGM electrolyte, and $\text{La}_{0.8}\text{Sr}_{0.2}\text{MnO}_3$ (LSM) cathode showed a peak power density of $\sim 150 \text{ mW cm}^{-2}$ at $800 \text{ }^\circ\text{C}$, which was much lower than that obtained in the present study because the LSM cathode showed a low catalytic activity at $800 \text{ }^\circ\text{C}$. Joo et al. reported that the cell assembled with $20 \text{ }\mu\text{m}$ LSGM electrolyte, which was prepared by the slurry coating method, showed a peak power density of 930 mW cm^{-2} at $700 \text{ }^\circ\text{C}$ ¹⁸. It means that the cell performance can be further improved by the decreasing of electrolyte thickness. However, the cell in their study had a very small active electrode area (diameter of only $\sim 2 \text{ mm}$) and it is difficult to scale up to large cells.

The performance of the cells assembled from plasma-sprayed LSGM electrolyte membranes may be further enhanced by the following approaches. First, the conductivity of plasma-sprayed LSGM electrolyte may be improved further to a value close to 100% of the bulk value by decreasing the non-bonded interfaces and porosity. For example, the deposition temperature can be increased, and dense spherical particles with a larger particle size than $30 \text{ }\mu\text{m}$ may be used. Then, the thickness of electrolyte can be decreased to $20\text{--}30 \text{ }\mu\text{m}$. Finally, since the electrode polarization resistance of the cell B was $\sim 0.3 \text{ }\Omega \text{ cm}^2$, the cell performance may be further improved by enhancing electrode performance. For example, a composite cathode may provide more TPBs for the cathode reactions.

4. Conclusions

APS was applied to the preparation of LSGM electrolytes for IT-SOFCs. Ga evaporation during plasma spraying was observed. Results showed the dominant effects of powder size and spray distance on Ga evaporation. Ga evaporation mainly occurred when the powder particle size was less than $30 \text{ }\mu\text{m}$, and the spray distance was less than 70 mm . The Ga evaporation led to the formation of Ga-deficient splats and LaSrGaO_4 phase, dramatically reducing ionic conductivity of LSGM deposit. It was also found that

the interlamellar bonding ratio (or interfacial connectivity) can be well controlled by depositing LSGM at a deposition temperature of about 300 °C. The simulation and experimental results revealed that the remarkable Ga evaporation can be well explained by a model involving vortex convection of melt within the fully molten droplets. This model has provided guidance in optimization of APS conditions for deposition of dense LSGM electrolyte membranes from a powder with a particle size of >30 μm. The improved LSGM electrolyte membranes have a pure phase, good interface connectivity (>80%), and low porosity (or high density), demonstrating an ionic conductivity of ~0.075 S cm⁻¹ at 800 °C, which is more than 78% of the bulk conductivity and ~17 times of that for the un-optimized LSGM deposit. Test cells assembled with the improved LSGM electrolyte membranes showed a peak power density of 712 mW cm⁻² at 800 °C, suggesting that the atmospheric plasma spray is promising approach to cost-effective fabrication of IT-SOFCs.

Acknowledgments

This study was partially supported by the National Basic Research Program (Grant No. 2012CB625100, 50671080).

References

1. S. G. Singhal and K. Kendall, *High Temperature Solid Oxide Fuel Cells: Fundamentals, Design and Application*, Elsevier, 2004.
2. L. Yang, Y. Choi, W. Qin, H. Chen, K. Blinn, M. Liu, P. Liu, J. Bai, T. A. Tyson and M. Liu, *Nat. Commun.*, 2011, **2**, 357.
3. L. Yang, S. Z. Wang, K. Blinn, M. F. Liu, Z. Liu, Z. Cheng and M. L. Liu, *Science*, 2009, **326**, 126–129.

4. M. Liu, Y. Choi, L. Yang, K. Blinn, W. Qin, P. Liu and M. Liu, *Nano Energy*, 2012, **1**, 448–455.
5. D. Ding, X. Li, S. Lai, K. Gerdes and M. Liu, *Energy and Environ. Sci.* 2014, **7**, 552–575.
6. M. Liu, M. E. Lynch, K. Blinn, F. M. Alamgir and Y. Choi, *Mater. Today*, 2011, **14**, 534–546.
7. A. J. Jacobson, *Chem. Mater.*, 2009, **22**, 660–674.
8. A. Aguadero, L. Fawcett, S. Taub, R. Woolley, K. T. Wu, N. Xu, J. Kilner and S. Skinner, *J. Mater. Sci.*, 2012, **47**, 3925–3948.
9. Q. Zhen, G. M. Kale, W. He and J. Liu, *Chem. Mater.*, 2006, **19**, 203–210.
10. P. Singh and J. B. Goodenough, *J. Am. Chem. Soc.*, 2013, **135**, 10149–10154.
11. T. Ishihara, H. Matsuda and Y. Takita, *J. Am. Chem. Soc.*, 1994, **116**, 3801–3803.
12. T. Ishihara, J. A. Kilner, M. Honda and Y. Takita, *J. Am. Chem. Soc.*, 1997, **119**, 2747–2748.
13. J. H. Kim and H. I. Yoo, *Solid State Ionics*, 2001, **140**, 105–113.
14. Y. Arachi, H. Sakai, O. Yamamoto, Y. Takeda and N. Imanishai, *Solid State Ionics*, 1999, **121**, 133–139.
15. P. S. Cho, S. Y. Park, Y. H. Cho, S. J. Kim, Y. C. Kang, T. Mori and J. H. Lee, *Solid State Ionics*, 2009, **180**, 788–791.
16. P. Majewski and T. Maldener, *Int. J. Appl. Ceram. Technol.*, 2009, **6**, 249–256.
17. K. Kawahara, S. Suda, M. Suzuki, M. Kawano, H. Yoshida and T. Inagaki, *Solid State Ionics*, 2009, **180**, 236–240.
18. J. H. Joo, D. Y. Kim and G. M. Choi, *Solid State Ionics*, 2011, **192**, 523–526.
19. X. Zhang, S. Ohara, R. Maric, H. Okawa, T. Fukui, H. Yoshida, T. Inagaki and K. Miura, *Solid State Ionics*, 2000, **133**, 153–160.
20. B. Huang, S. R. Wang, R. Z. Liu, X. F. Ye, H. W. Nie, X. F. Sun and T. L. Wen, *J. Power Sources*,

- 2007, **167**, 39–46.
21. J. Peña-Martínez, D. Marrero-López, J. C. Ruiz-Morales, C. Savaniu, P. Núñez and J. T. S. Irvine, *Chem. Mater.*, 2006, **18**, 1001–1006.
22. S. B. Ha, Y. H. Cho, H. I. Ji, J. H. Lee, Y. C. Kang and J. H. Lee, *J. Power Sources*, 2011, **196**, 2971–2978.
23. T. Ishihara, H. Eto and J. Yan, *Int. J. Hydrogen Energy*, 2011, **36**, 1862–1867.
24. K. Sasaki, M. Muranaka, A. Suzuki and T. Terai, *Solid State Ionics*, 2008, **179**, 1268–1272.
25. R. Hui, Z. Wang, O. Kesler, L. Rose, J. Jankovic, S. Yick, R. Maric and D. Ghosh, *J. Power Sources*, 2007, **170**, 308–323.
26. Y. Z. Xing, C. J. Li, C. X. Li and G. J. Yang, *J. Power Sources*, 2008, **176**, 31–38.
27. C. X. Li, C. J. Li and G. J. Yang, *J. Therm. Spray Tech.*, 2009, **18**, 83–89.
28. S. L. Zhang, C. X. Li, C. J. Li, G. J. Yang and Z. H. Han, *J. Power Sources*, 2013, **232**, 123–131.
29. C. X. Li, C. J. Li and L. J. Guo, *Int. J. Hydrogen Energy*, 2010, **35**, 2964–2969.
30. M. Poon and O. Kesler, *J. Power Sources*, 2012, **210**, 204–217.
31. B. D. White, O. Kesler and L. Rose, *J. Power Sources*, 2008, **178**, 334–343.
32. C. Hwang, C. H. Tsai, C. H. Lo and C. H. Sun, *J. Power Sources*, 2008, **180**, 132–142.
33. X. Q. Ma, H. Zhang, J. Dai, J. Roth, R. Hui, T. D. Xiao and D. E. Reisner, *J. Therm. Spray Tech.*, 2005, **14**, 61–66.
34. C. X. Li, Y. X. Xie, C. J. Li and G. J. Yang, *J. Power Sources*, 2008, **184**, 370–374.
35. C. X. Li, C. J. Li, H. G. Long, Y. Z. Xing, X. J. Ning, C. Zhang, H. L. Liao and C. Coddet, *Solid State Ionics*, 2006, **177**, 2149–2153.
36. R. Huang, H. Fukunuma, Y. Uesugi and Y. Tanaka, *J. Therm. Spray Tech.*, 2012, **21**, 636–643.

37. H. Renzhong, H. Fukanuma, Y. Uesugi and Y. Tanaka, Plasma Science, *IEEE T. plasma Sci.*, 2011, **39**, 1974–1982.
38. H. Renzhong, Doctor Thesis, Kanazawa University, 2012.
39. Y. P. Wan, V. Prasad, G. X. Wang, S. Sampath and J. R. Fincke, *J. Heat Transfer*, 1999, **121**, 691–699.
40. S. L. Zhang, C. X. Li and C. J. Li, *J. Power Sources*, 2014, **264**, 195–205.
41. W. Kuncewicz-Kupczyk, D. Kobertz, M. Miller, C. Chatillon, L. Singheiser and K. Hilpert, *J. Am. Ceram. Soc.*, 2002, **85**, 2299–2305.
42. W. Kuncewicz-Kupczyk, D. Kobertz, M. Miller, L. Singheiser and K. Hilpert, *J. Electrochem. Soc.*, 2001, **148**, E276–E281.
43. G. Espie, A. Denoirjean, P. Fauchais, J. C. Labbe, J. Dubsky, O. Schneeweiss and K. Volenik, *Surf. Coat. Technol.*, 2005, **195**, 17–28.
44. A. A. Syed, A. Denoirjean, P. Denoirjean, J. C. Labbe and P. Fauchais, *J. Therm. Spray Tech.*, 2005, **14**, 117–124.
45. S. Hao, C. J. Li and G.-J. Yang, *J. Therm. Spray Tech.*, 2011, **20**, 160–169.
46. C. J. Li, G. J. Yang and C. X. Li, *J. Therm. Spray Tech.*, 2013, **22**, 192–206.
47. G. J. Yang, C. X. Li, S. Hao, Y. Z. Xing, E. J. Yang and C. J. Li, *Surf. Coat. Technol.*, 2013, **235**, 841–847.
48. D. Marrero-López, J. C. Ruiz-Morales, J. Peña-Martínez, M. C. Martín-Sedeño and J. R. Ramos-Barrado, *Solid State Ionics*, 2011, **186**, 44–52.
49. Y. Z. Xing, C. J. Li, Q. Zhang, C. X. Li and G. J. Yang, *J. Am. Ceram. Soc.*, 2008, **91**, 3931–3936.
50. Raghvendra, R. Kumar Singh and P. Singh, *Ceram. Int.*, 2014, **40**, 7177–7184.

51. V. Sarıboğa, H. Özdemir and M. A. F. Öksüzömer, *J. Eur. Ceram. Soc.*, 2013, **33**, 1435–1446.

Table and Figure captions

Table 1 Typical plasma spray parameters (LSCF = $\text{La}_{0.6}\text{Sr}_{0.4}\text{Co}_{0.2}\text{Fe}_{0.8}\text{O}_3$)

Table 2 Properties of LSGM particles utilized in simulation

Table 3 Performance of LSGM electrolytes prepared by APS and SPS in the literature

Fig. 1 Typical morphologies of powders A (a) and B (b) and their particle size distribution (c)

Fig. 2 Computational domains of (a) plasma torch and (b) plasma jet

Fig. 3 Surface morphologies of LSGM splats deposited on polished YSZ substrate at a spray distance of 90 mm

Fig. 4 (a) Molar ratio of Ga to La for different size splats at different spray distances; (b) Effect of spray distance and particle size on Ga evaporation

Fig. 5 Plasma gas temperature (a) and (b) velocity distribution inside the torch; gas temperature (c) and (d) velocity distribution of the plasma jet

Fig. 6 In-flight particle (a) velocity, (b) surface temperature, (c) core temperature and (d) melting degree for particles with different sizes

Fig. 7 Schematic diagram of the evaporation process for the particles in the plasma jet

Fig. 8 The simulated temperature and velocity compared with the experiment results for 10 μm particle,

(a) In-flight particle temperature (b) particle and plasma gas velocity

Fig. 9 Surface morphologies of the fractured LSGM splats; (a) Ga-deficient splat (type I); (b) with Ga-deficient shell (type II); (c) without Ga evaporation (type III)

Fig. 10 Microstructure of the LSGM deposit prepared by powder A at a deposition temperature less than 150 $^{\circ}\text{C}$, (a) polished cross-section, (b) fractured cross-section

Fig. 11 Microstructure of the LSGM deposits prepared by powder A at a deposition temperature of ~300–350 °C, (a) polished cross-section, (b) fractured cross-section

Fig. 12 (a) Microstructure of the polished cross-section of the as-sprayed LSGM electrolyte prepared by powder A. (b) EDX line scans of La, Sr, Ga, and Mg across the region as marked in Fig. 12 (a). (c) Fractured cross-section of the as-sprayed LSGM electrolyte prepared by powder A. (d) Microstructure of the annealed deposit prepared by powder A

Fig. 13 TEM images of the cross-section of the as-sprayed LSMG electrolyte prepared by powder A. (a) bright-field image, (b) EDX maps of the region marked by dotted box in (a), (c) electron diffraction image of the region marked as A in (a), (d) HR-TEM image of the crystalline and amorphous regions (marked by arrows B in (a))

Fig. 14 TEM images of the cross-section of the as-sprayed LSMG electrolyte prepared by powder A, (a) bright-field image of the region without Ga evaporation, (b) electron diffraction image of the region marked as A in (a)

Fig. 15 Microstructures of the (a) polished cross-section and (b) fractured cross-section of the as-sprayed LSGM deposits prepared by powder B with a size of >30 μm

Fig. 16 XRD patterns of LSGM electrolytes, (a) prepared by powder A, (b) prepared by powder B

Fig. 17 EBSD maps for annealed LSGM deposit. (a) Orientation map of Euler angle; (b) Phase distribution map

Fig. 18 Schematic diagram of the microstructural developments of plasma sprayed LSGM electrolyte by different spraying routes. (a) deposited from powder A without preheating, (b) deposited from powder A with preheating, (c) deposited from powder B with preheating. A is nonbonded interface, B is vertical cracks, C is closed pores, D is the Ga-evaporated region, and E is the LaSrGaO₄ phase

Fig. 19 (a) Morphologies of the fractured cross-section of sintered LSGM bulk, (b) thermal conductivities of LSGM bulk and deposits

Fig. 20 Electrochemical impedance spectra for (a) sintered bulk, (b) deposits prepared by powder A and (c) deposits prepared by powder B at different temperatures

Fig. 21 (a) Total ionic conductivity of LSGM bulk and deposits, (b) Arrhenius plots of the total conductivity for LSGM bulk and deposits

Fig. 22 (a) Cross-section of the fractured SOFC single cell, (b) microstructure of plasma-sprayed LSCF cathode and the interface between cathode and electrolyte

Figure 23 Output performance of the single cell: (a) with the electrolyte prepared by powder A and (b) with the electrolyte prepared by powder B; (c) impedance spectra obtained for the cells at 800 °C under the OCV conditions

Fig. 24 (a) Schematic diagrams for the interfaces and TPBs between cathode and electrolytes prepared by different powders, (a) powder A, (b) powder B

Table 1 Typical plasma spray parameters (LSCF = $\text{La}_{0.6}\text{Sr}_{0.4}\text{Co}_{0.2}\text{Fe}_{0.8}\text{O}_3$)

Parameter	Unit	LSGM electrolyte	LSCF cathode
Plasma arc power	kW	24	30
Arc voltage	V	40	50
Arc current	A	600	550
Flow rate of Ar	slpm	50	50
Flow rate of H_2	slpm	–	1.5
Powder feed rate	g min^{-1}	25	25
Deposition temperature	$^{\circ}\text{C}$	<150 and 300–350	<150
Spray distance	mm	–	100
Thickness	μm	50–55	20–30

Table 2 Properties of LSGM particles utilized in simulation

Parameter	Unit	Value
Density	kg m^{-3}	6,000
Specific heat $C_p(T)$	$\text{J kg}^{-1} \text{K}^{-1}$	$T < 2,000 \text{ K}$, $C_p(T) = -1.17 \times 10^{-4} T^2 + 0.3698 T + 406.1$ $T > 2,000 \text{ K}$, $C_p(T) = 650$
Thermal conductivity $\lambda(T)$	$\text{W m}^{-1} \text{K}^{-1}$	$T < 2,000 \text{ K}$, $\lambda(T) = 7.145 \times 10^{-7} T^2 - 5.24 T + 0.03274$ $T > 2,000 \text{ K}$, $\lambda(T) = 2.5$
Latent heat	kJ kg^{-1}	1,000
Melting point	K	2,000

Table 3 Performance of LSGM electrolytes prepared by APS and SPS in the literature

Reference	Method	Preparation condition	Conductivity (S cm^{-1}) /800 $^{\circ}\text{C}$
Li et al. ³⁴	APS	Powder size: $d_{50} = \sim 20 \mu\text{m}$	0.008
Hwang et al. ³²	APS	Powder size: $d_{50} = 37 \mu\text{m}$	0.054
Present study	APS	Powder size: $d_{50} = 25 \mu\text{m}$	0.004
Present study	APS	Powder size: $d_{50} = 56 \mu\text{m}$	0.075
Raghvendra et al. ⁵⁰	SPS	1,400 $^{\circ}\text{C}/6 \text{ h}$	0.056
Saribođa et al. ⁵¹	SPS	1,400 $^{\circ}\text{C}/6 \text{ h}$	0.042
Marrero-Ló et al. ⁴⁸	SPS	1,300 $^{\circ}\text{C}/4 \text{ h}$ and 1,400 $^{\circ}\text{C}/4 \text{ h}$	0.052/0.095
Ha et al. ²²	SPS	1,300 $^{\circ}\text{C}/4 \text{ h}$ V_2O_5 as the additive	0.027/700 $^{\circ}\text{C}$

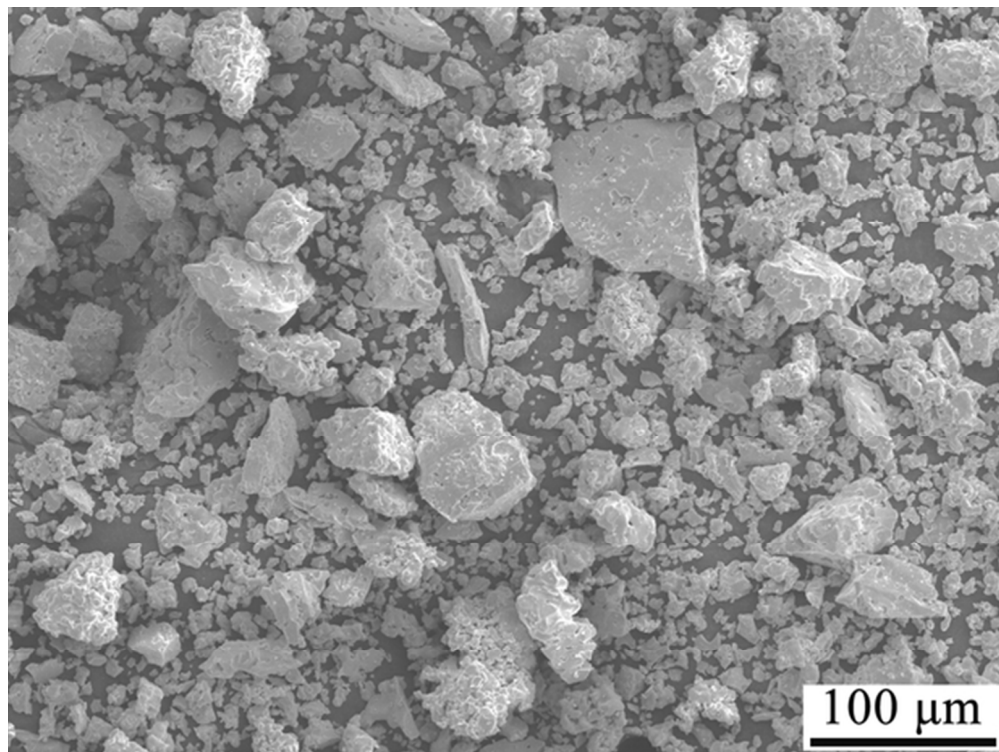


Fig. 1 (a) Typical morphologies of powders A
52x39mm (300 x 300 DPI)

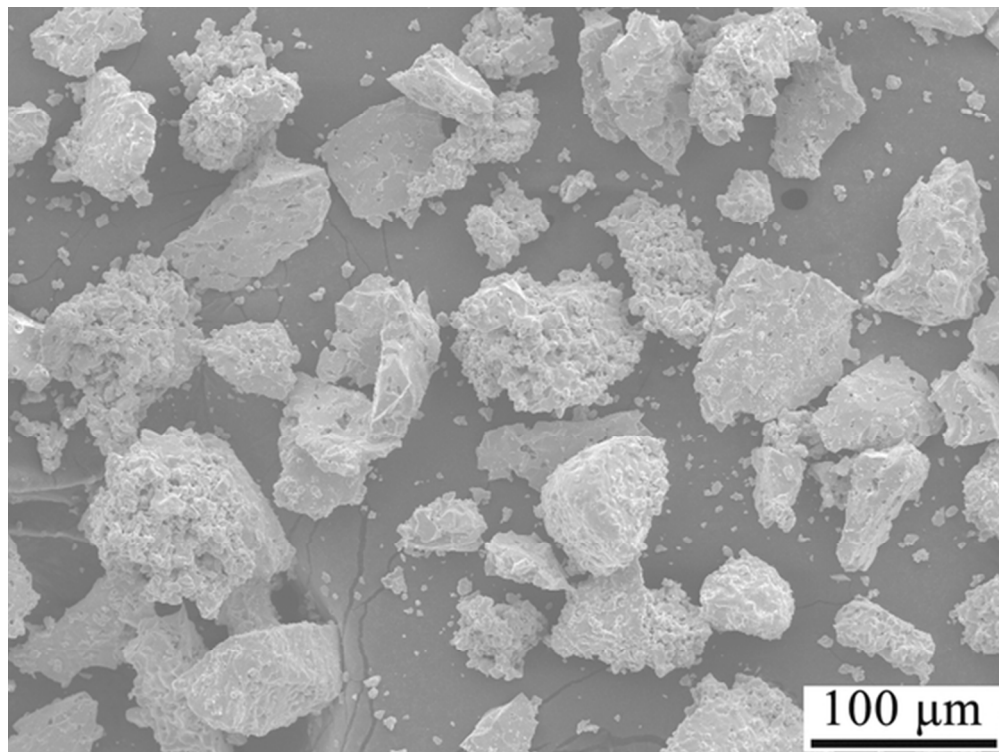


Fig. 1 (b) Typical morphologies of powders B
52x39mm (300 x 300 DPI)

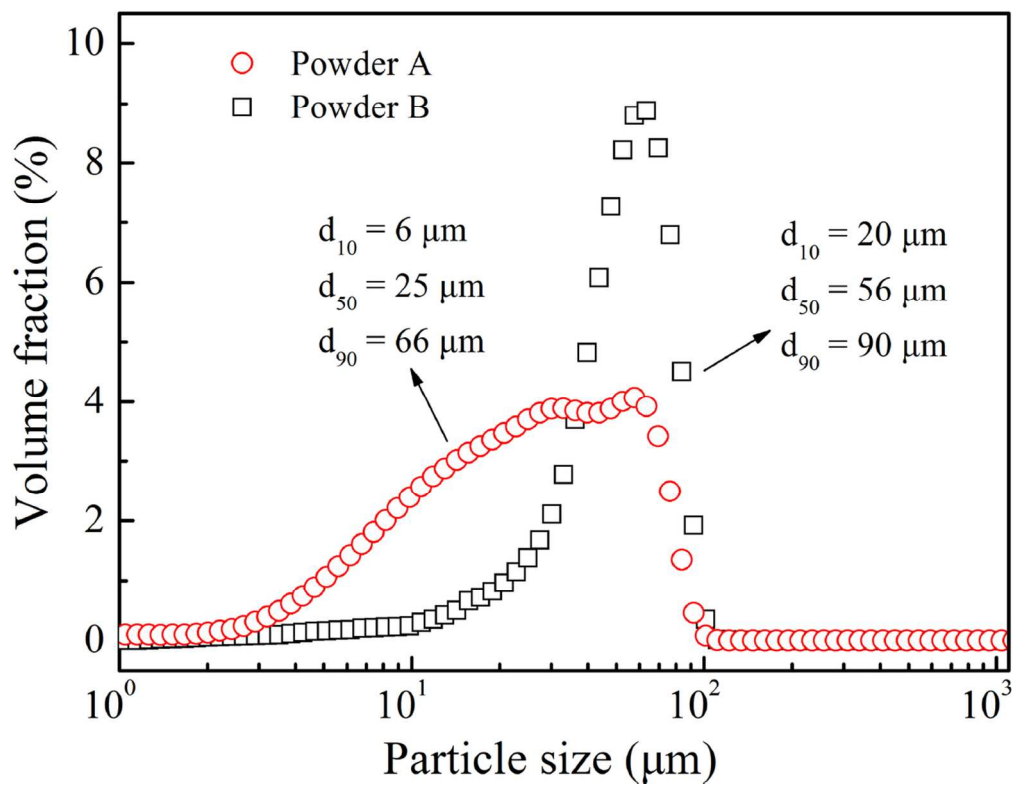


Fig. 1 (c) Particle size distribution
54x41mm (600 x 600 DPI)

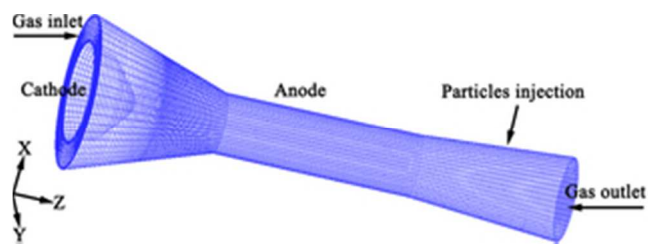


Fig. 2 (a) Computational domains of plasma torch
26x9mm (300 x 300 DPI)

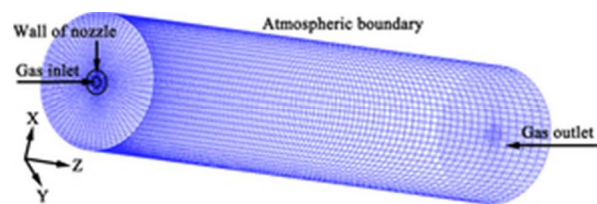


Fig. 2 (b) Computational domains of plasma jet
24x8mm (300 x 300 DPI)

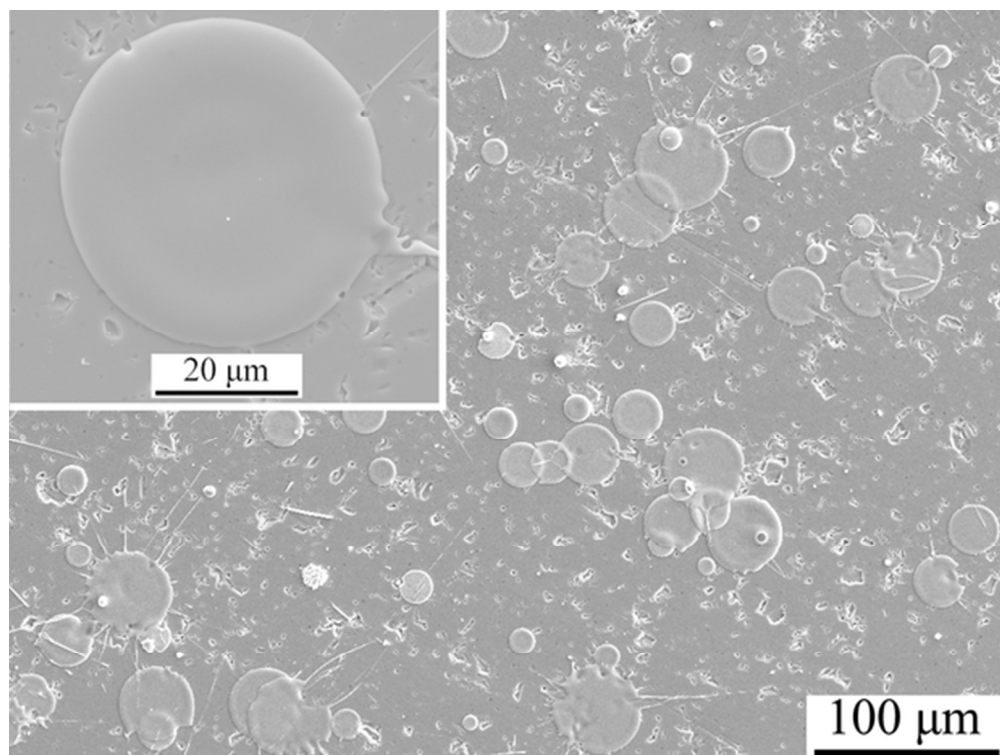


Fig. 3 Surface morphologies of LSGM splats deposited on polished YSZ substrate at a spray distance of 90 mm
52x39mm (300 x 300 DPI)

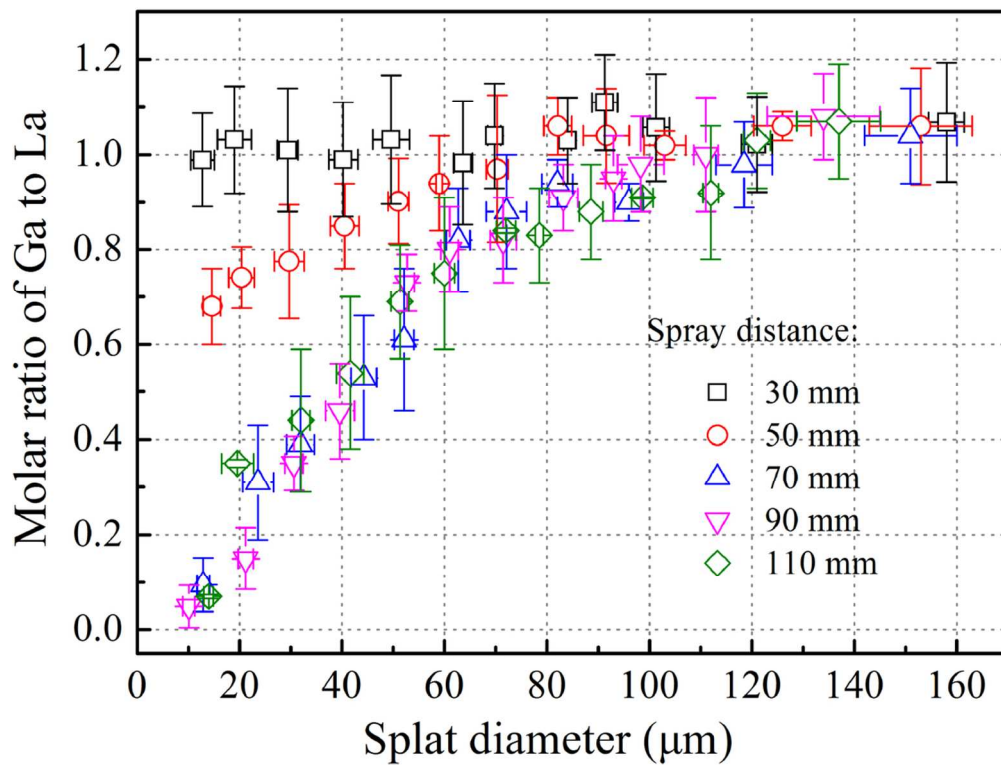


Fig. 4 (a) Molar ratio of Ga to La for different size splats at different spray distances 52x40mm (600 x 600 DPI)

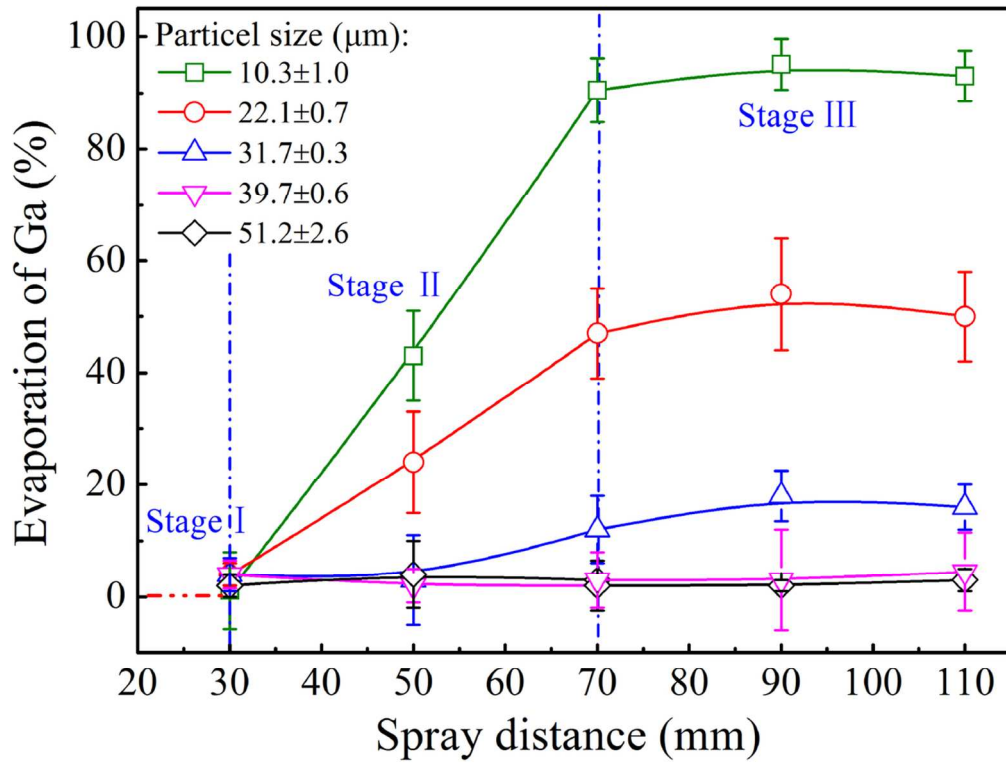


Fig. 4 (b) Effect of spray distance and particle size on Ga evaporation
52x40mm (600 x 600 DPI)

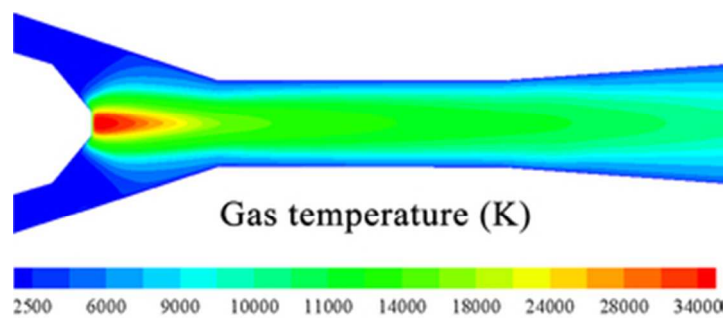


Fig. 5 (a) Plasma gas temperature inside the torch
29x12mm (300 x 300 DPI)

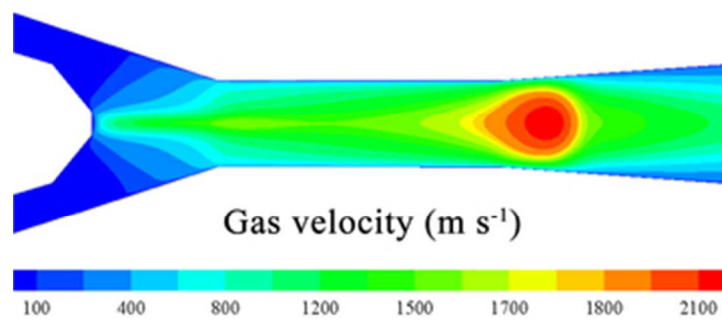


Fig. 5 (b) Plasma gas velocity distribution inside the torch
29x12mm (300 x 300 DPI)

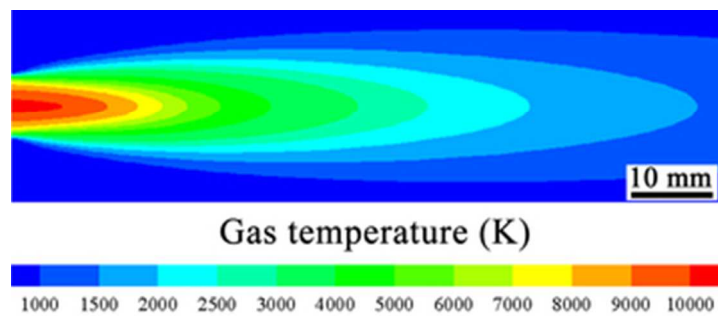


Fig. 5 (c) Gas temperature distribution of the plasma jet
29x12mm (300 x 300 DPI)

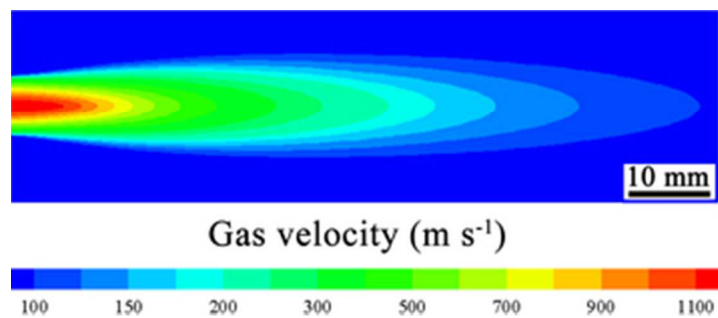


Fig. 5 (d) Gas velocity distribution of the plasma jet
29x12mm (300 x 300 DPI)

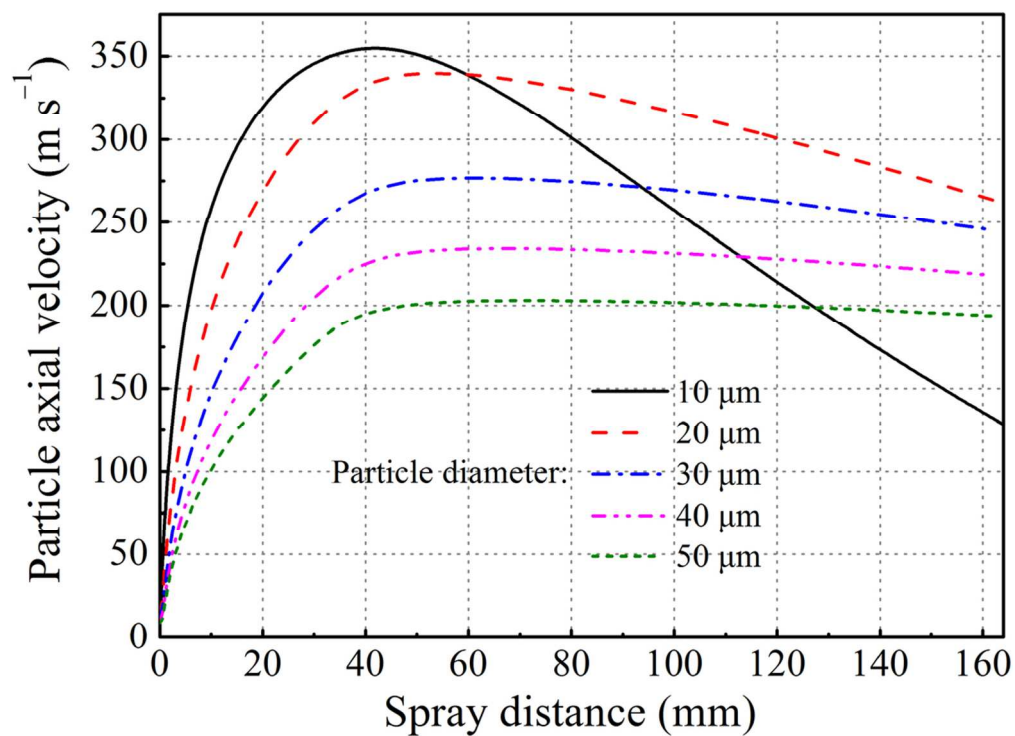


Fig. 6 (a) In-flight particle velocity with different sizes
50x36mm (600 x 600 DPI)

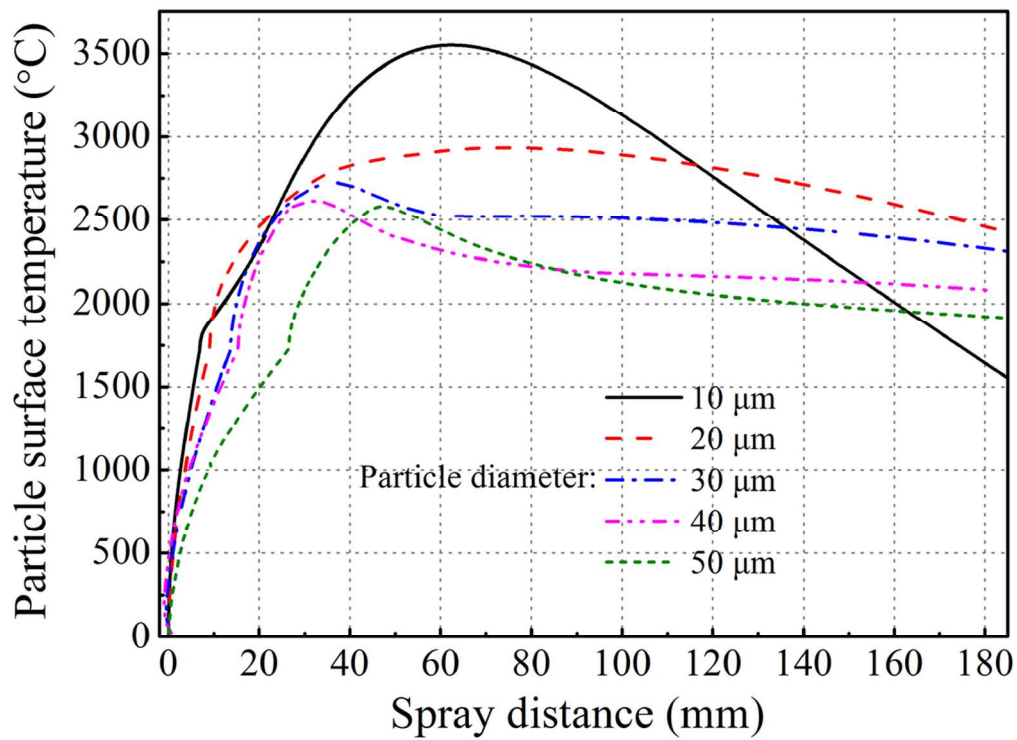


Fig. 6 (b) In-flight particle surface temperature for particles with different sizes
51x37mm (600 x 600 DPI)

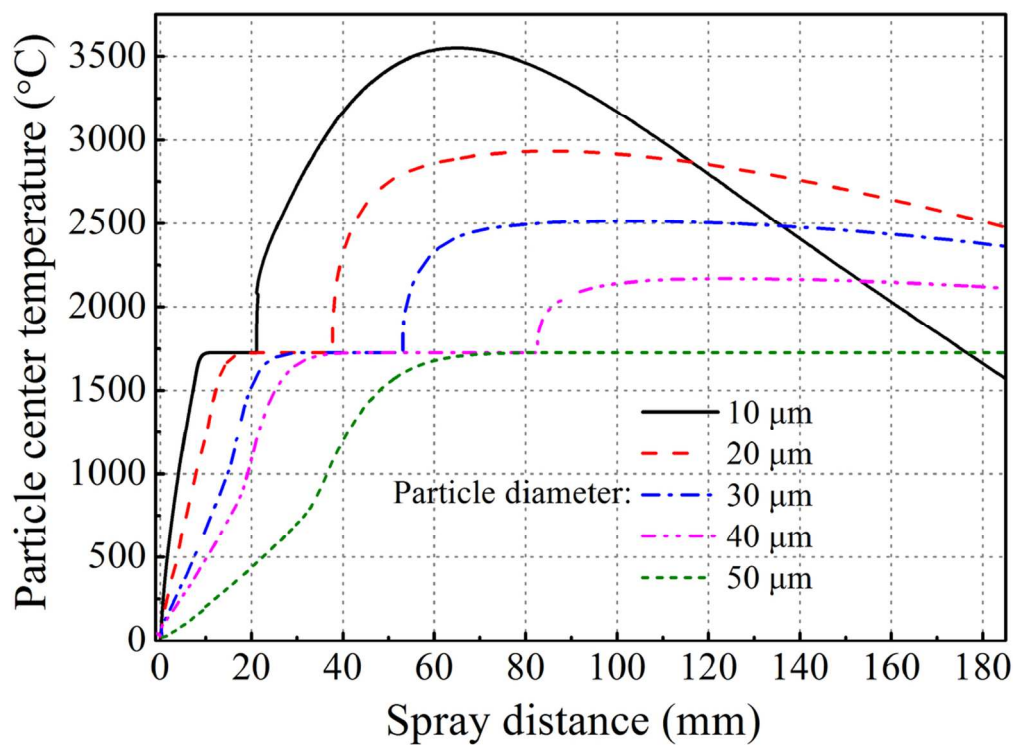


Fig. 6 (c) In-flight particle core temperature for particles with different sizes
51x37mm (600 x 600 DPI)

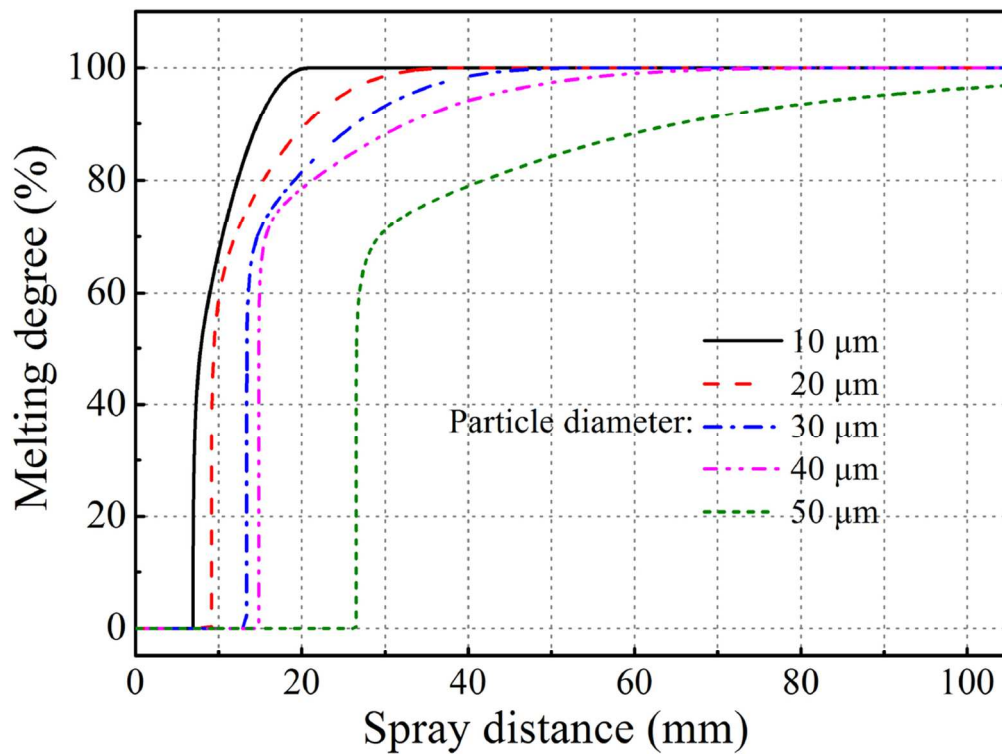


Fig. 6 (d) Melting degree for particles with different sizes
52x39mm (600 x 600 DPI)

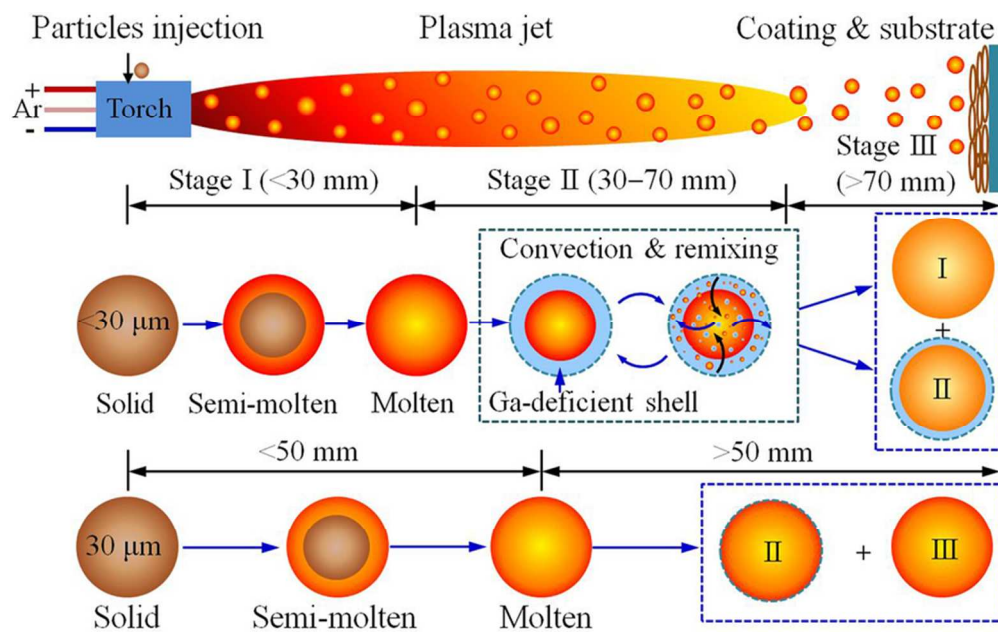


Fig. 7 Schematic diagram of the evaporation process for the particles in the plasma jet 80x49mm (300 x 300 DPI)

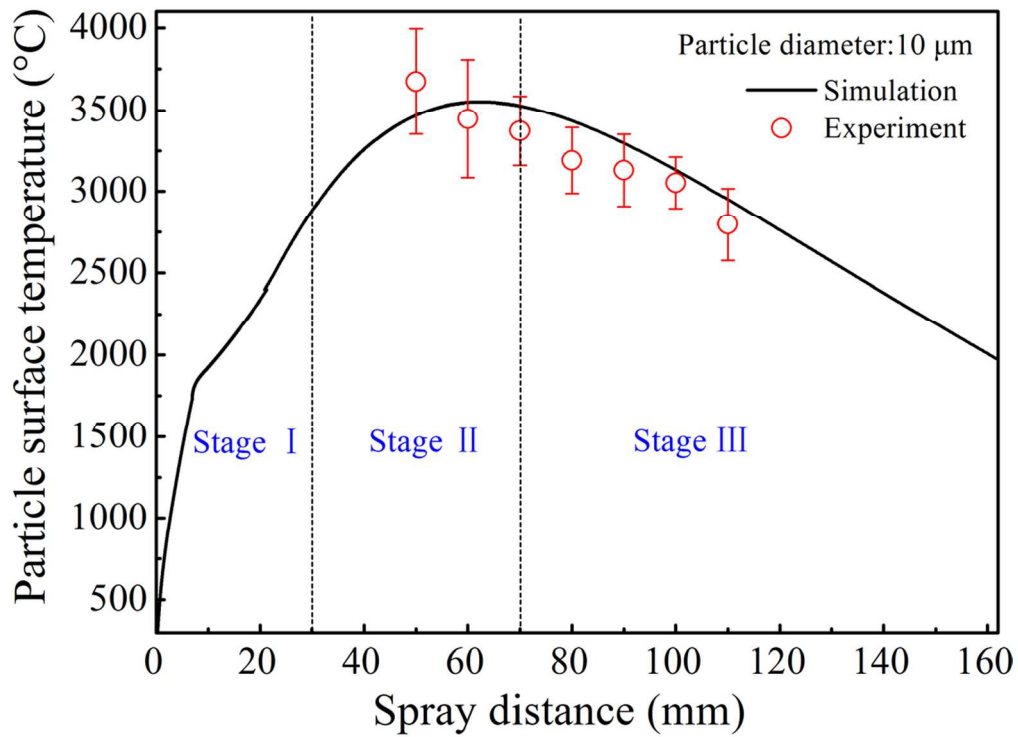


Fig. 8 (a) The simulated temperature for 10 μm particle compared with the experiment results 51x37mm (600 x 600 DPI)

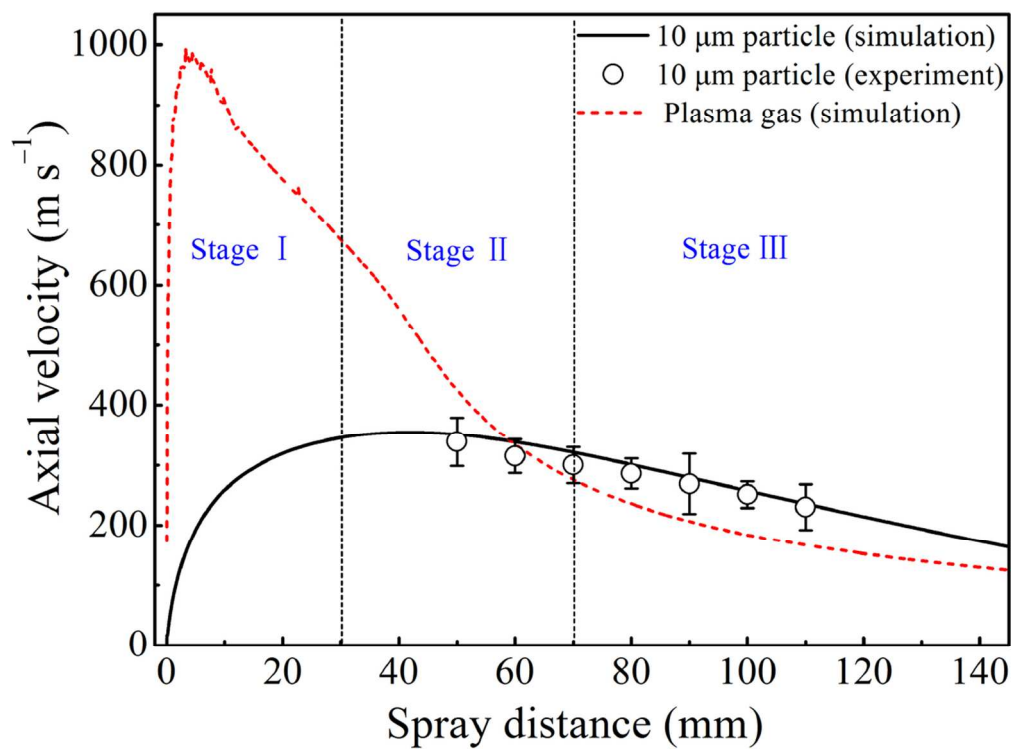


Fig. 8 (b) The simulated velocity for 10 μm particle and plasma gas compared with the experiment results
51x38mm (600 x 600 DPI)

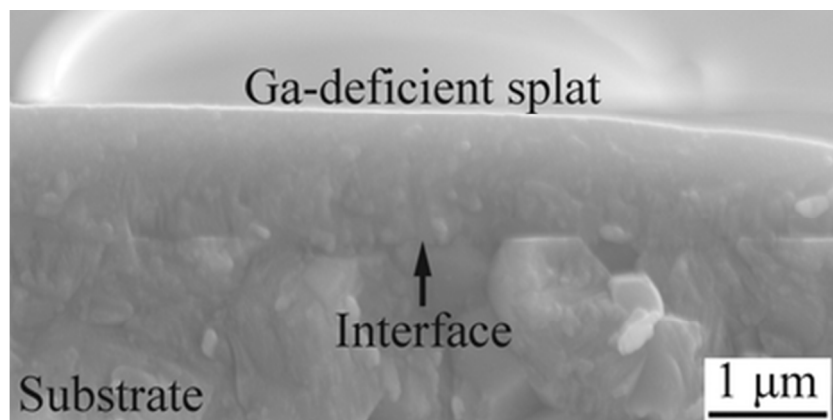


Fig. 9 (a) Surface morphologies of the fractured Ga-deficient LSGM splat (type I)
34x17mm (300 x 300 DPI)

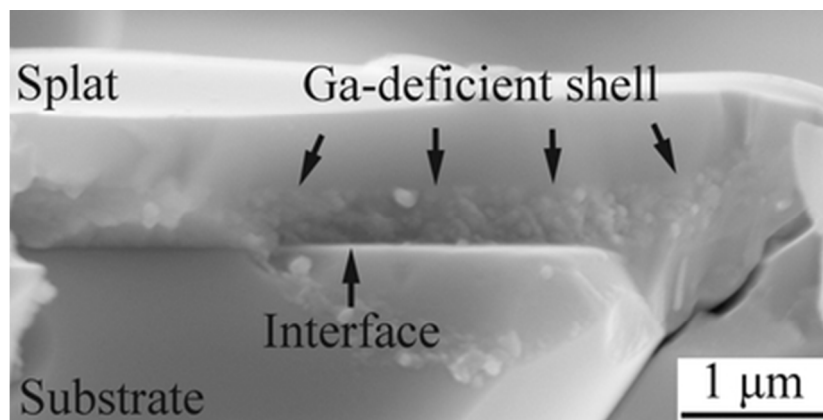


Fig. 9 (b) Surface morphologies of the fractured LSGM splats with Ga-deficient shell (type II)

34x17mm (300 x 300 DPI)

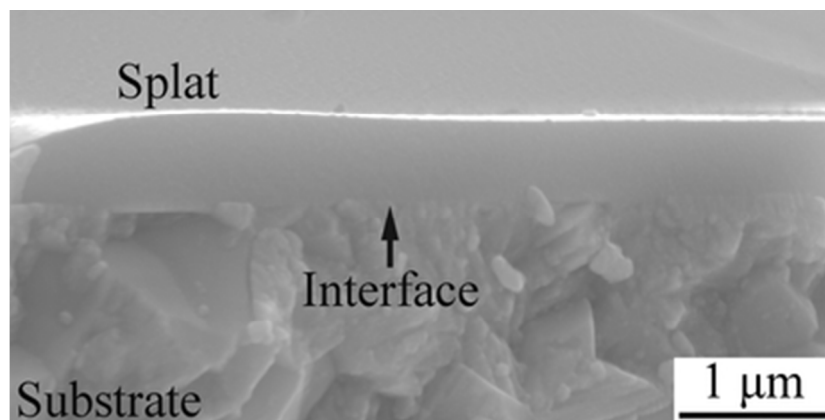


Fig. 9 (c) Surface morphologies of the fractured LSGM splats without Ga evaporation (type III)

34x17mm (300 x 300 DPI)

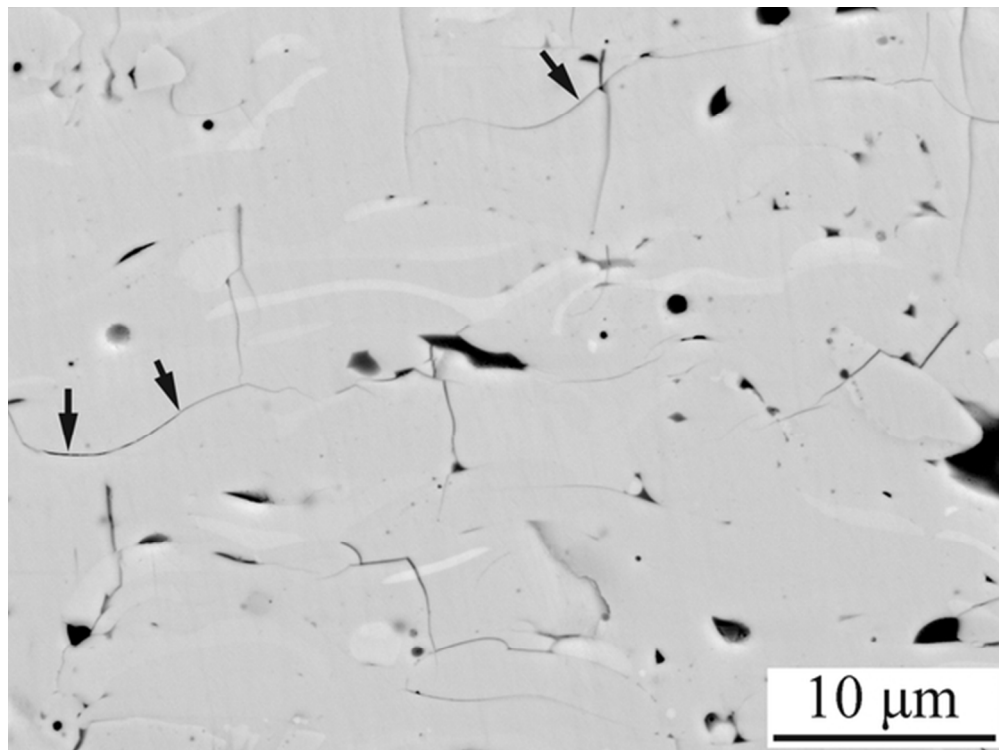


Fig. 10 (a) Microstructure of polished cross-section of the LSGM deposit prepared by powder A at a deposition temperature less than 150 °C
52x39mm (300 x 300 DPI)

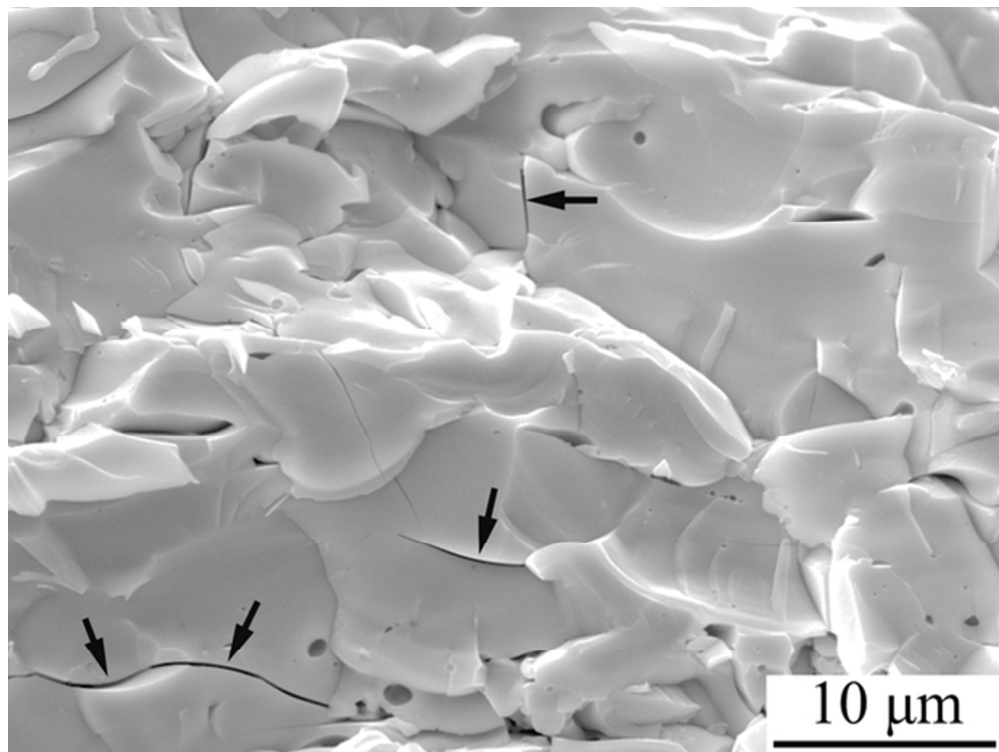


Fig. 10 (b) Microstructure of the fractured cross-section of LSGM deposit prepared by powder A at a deposition temperature less than 150 °C

52x39mm (300 x 300 DPI)

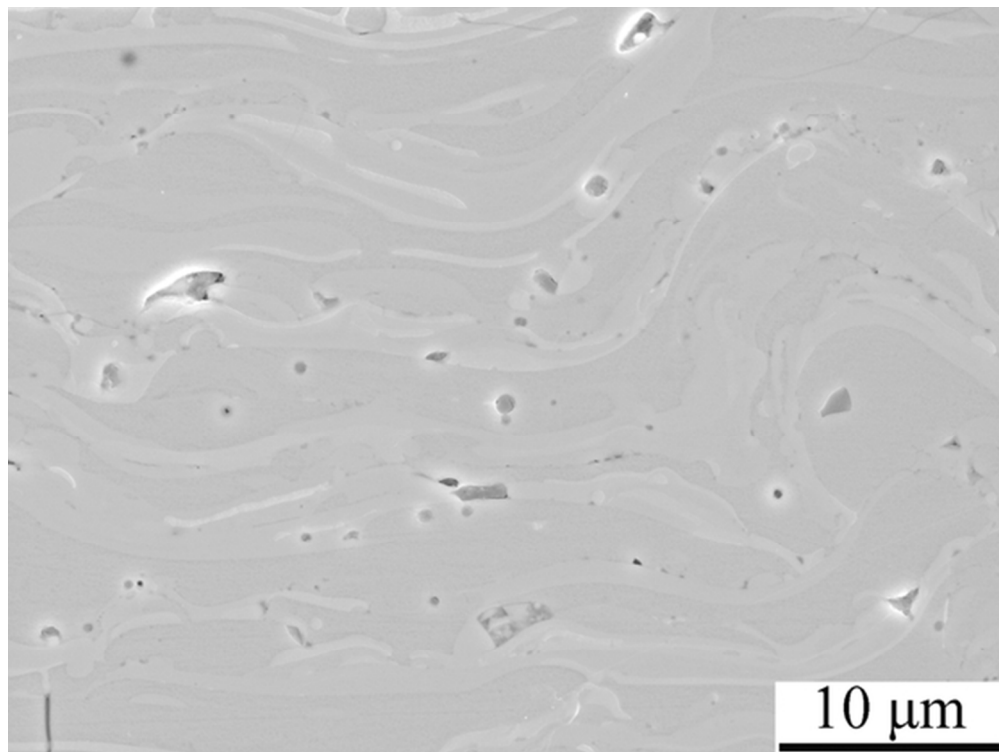


Fig. 11 (a) Microstructure of polished cross-section of the LSGM deposits prepared by powder A at a deposition temperature of $\sim 300\text{--}350\text{ }^{\circ}\text{C}$
52x39mm (300 x 300 DPI)

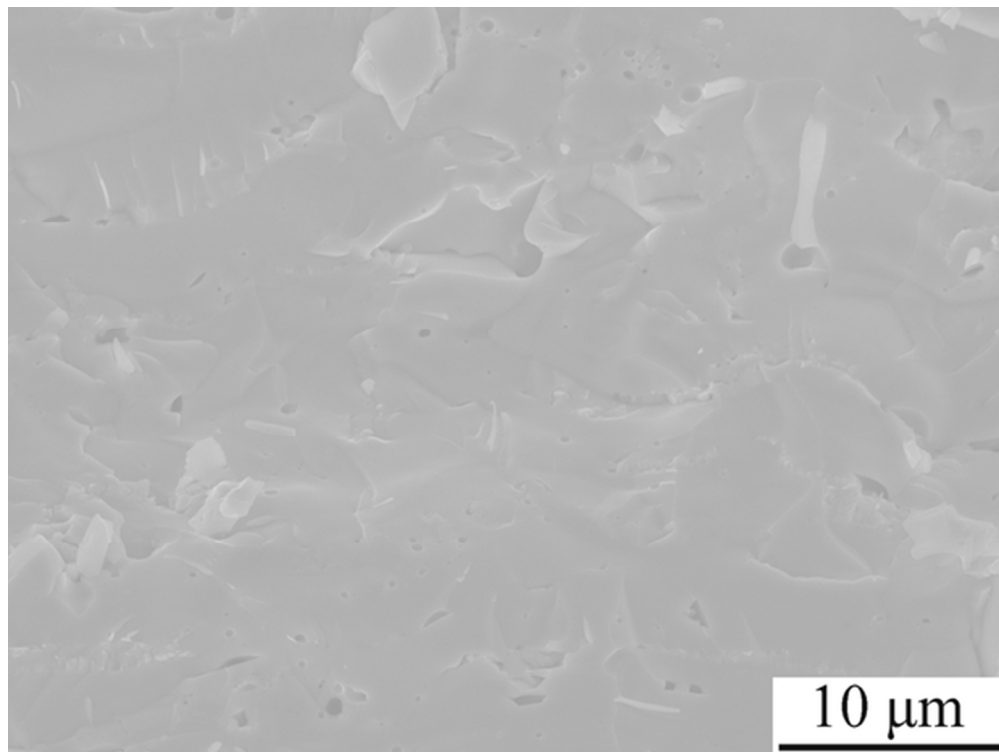


Fig. 11 (b) Microstructure of fractured cross-section of the LSGM deposits prepared by powder A at a deposition temperature of $\sim 300\text{--}350$ °C

52x39mm (300 x 300 DPI)

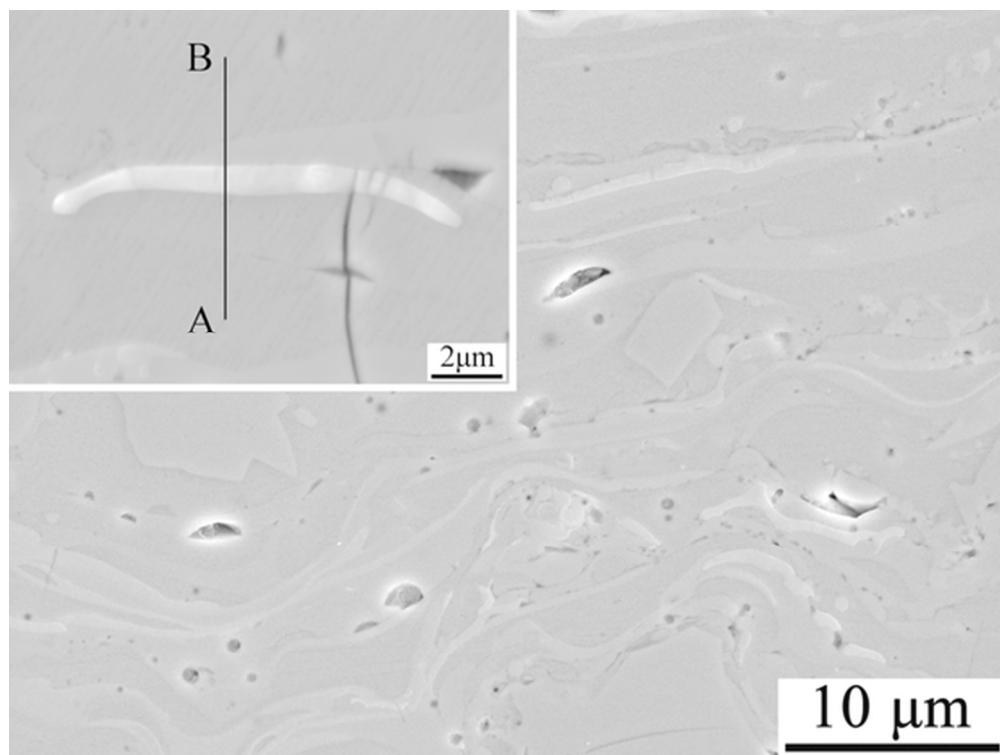


Fig. 12 (a) Microstructure of the polished cross-section of the as-sprayed LSGM electrolyte prepared by powder A.
52x39mm (300 x 300 DPI)

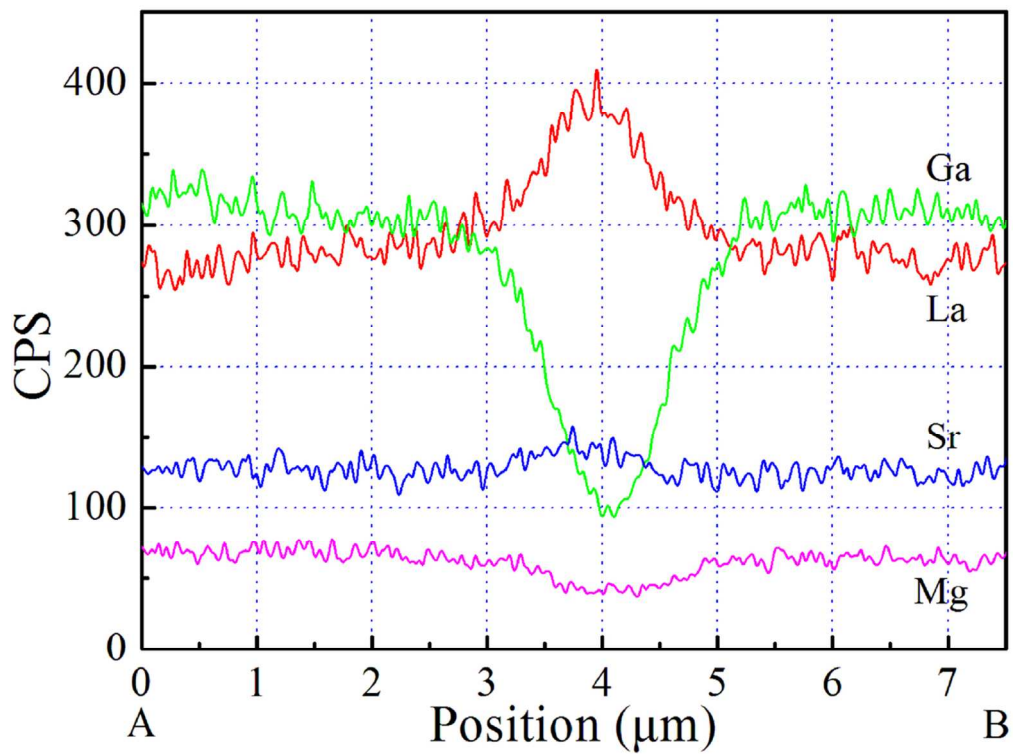


Fig. 12 (b) EDX line scans of La, Sr, Ga, and Mg across the region as marked in Fig. 12 (a)
52x39mm (600 x 600 DPI)

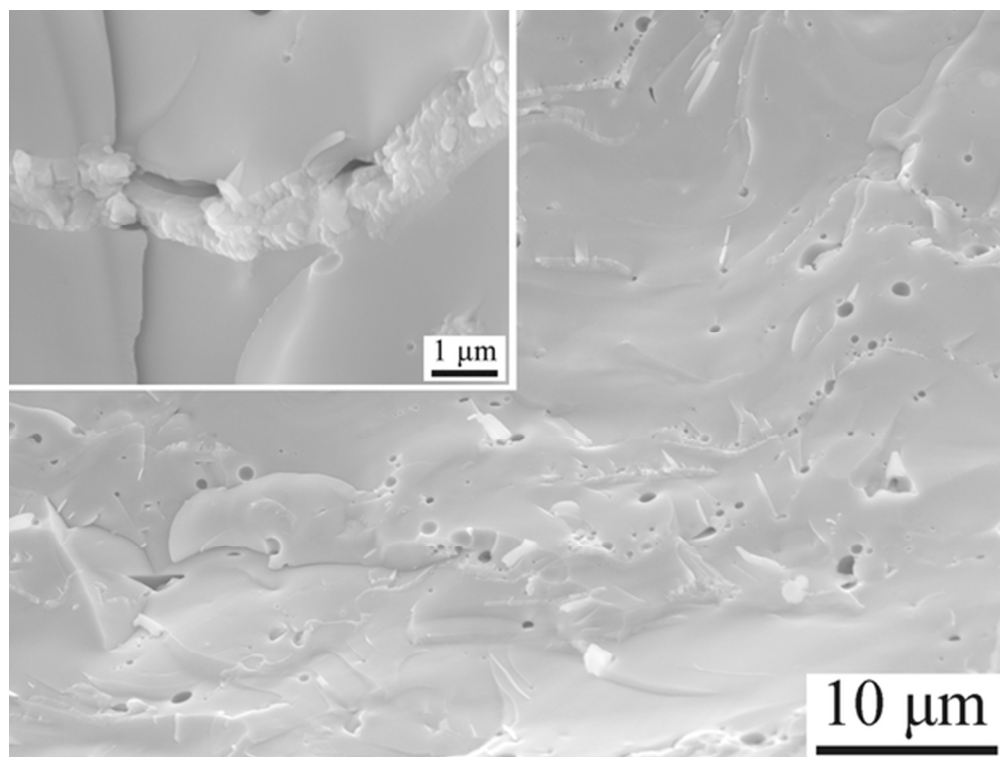


Fig. 12 (c) Fractured cross-section of the as-sprayed LSGM electrolyte prepared by powder A 52x39mm (300 x 300 DPI)

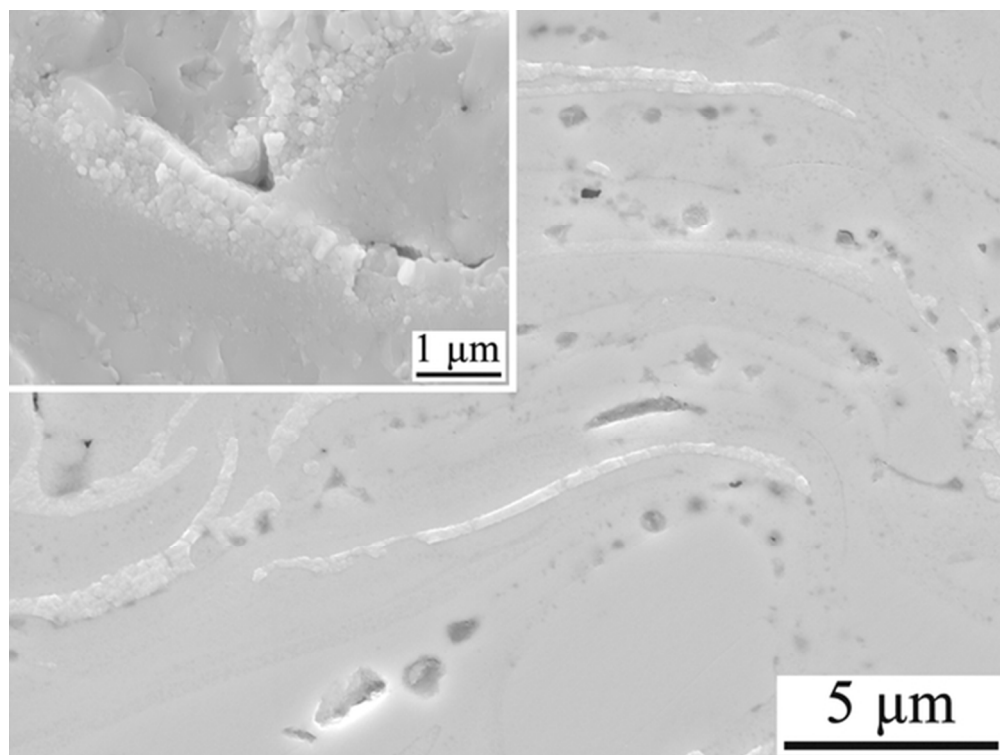


Fig. 12 (d) Microstructure of the annealed deposit prepared by powder A
52x39mm (300 x 300 DPI)

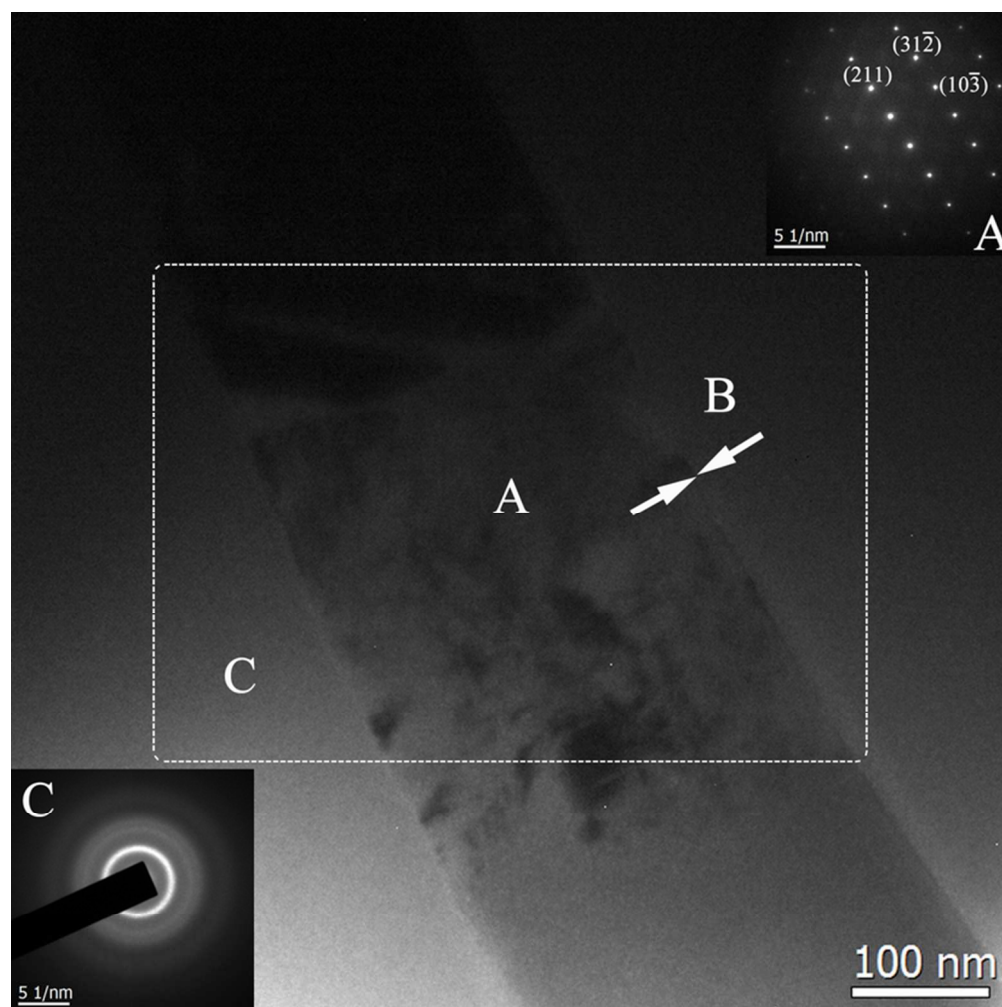


Fig. 13 (a) TEM image (bright-field image) of the cross-section of the as-sprayed LSMG electrolyte prepared by powder A.
70x70mm (300 x 300 DPI)

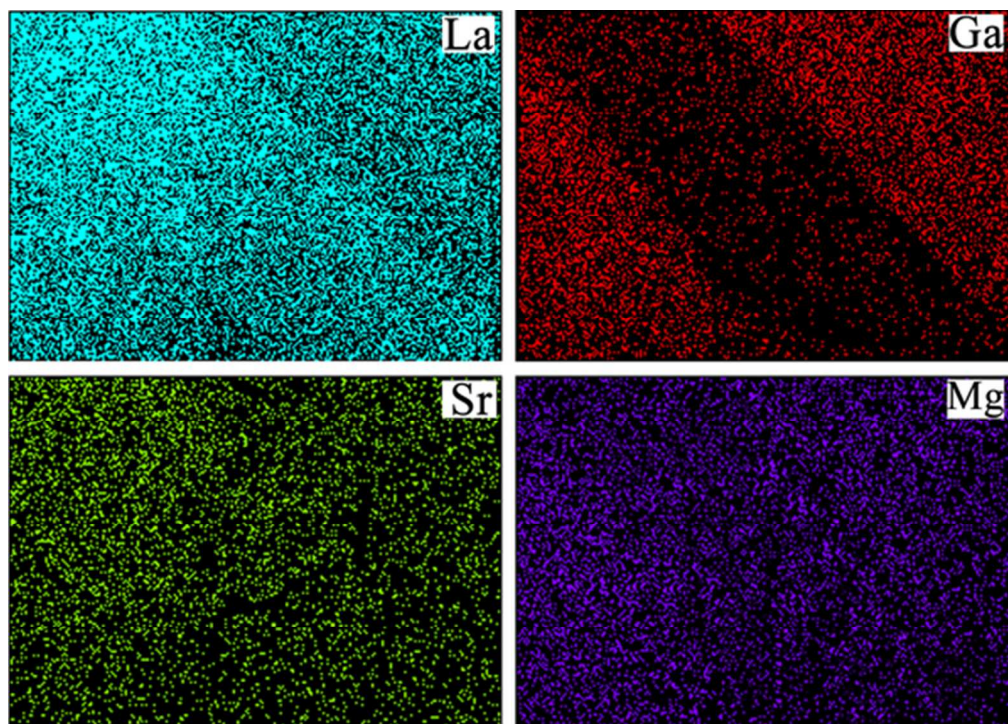


Fig. 13 (b) EDX maps of the region marked by dotted box in Fig. 13 (a)
50x36mm (300 x 300 DPI)

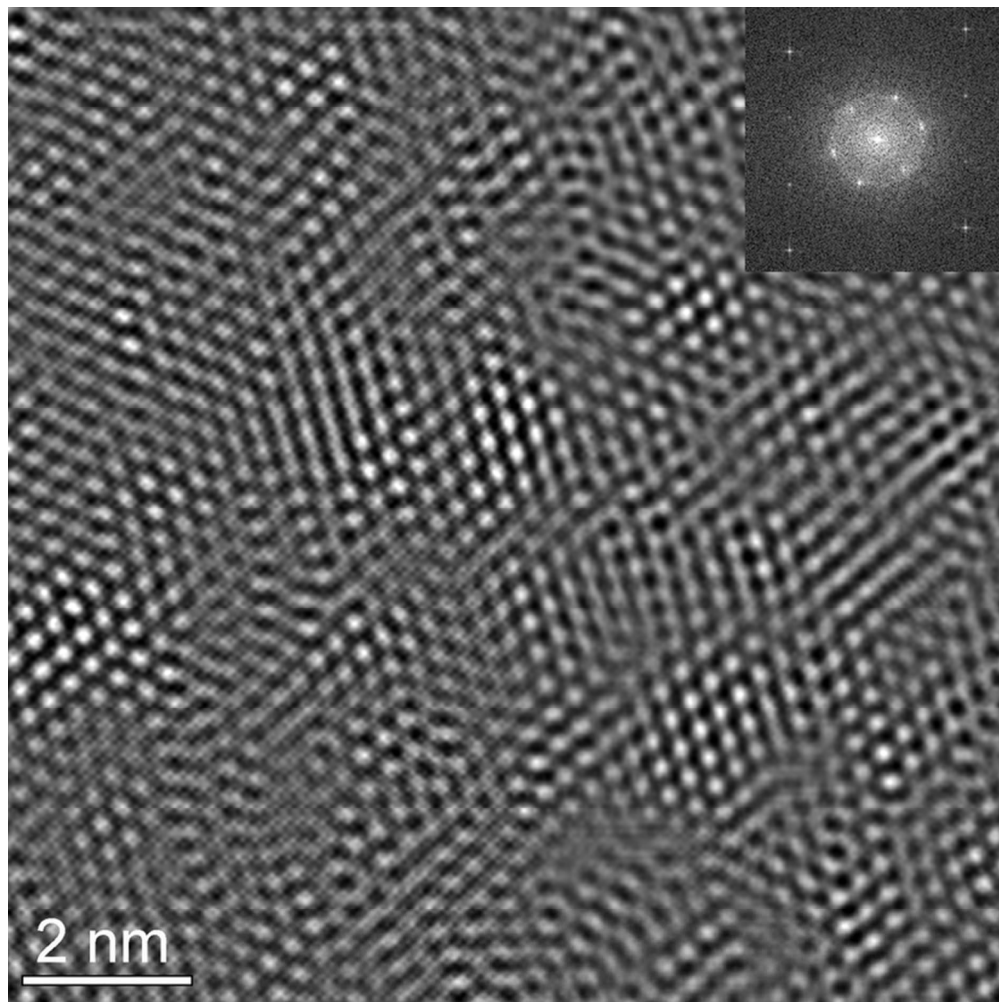


Fig. 13 (c) Electron diffraction image of the region marked as A in Fig. 13 (a)
70x70mm (300 x 300 DPI)

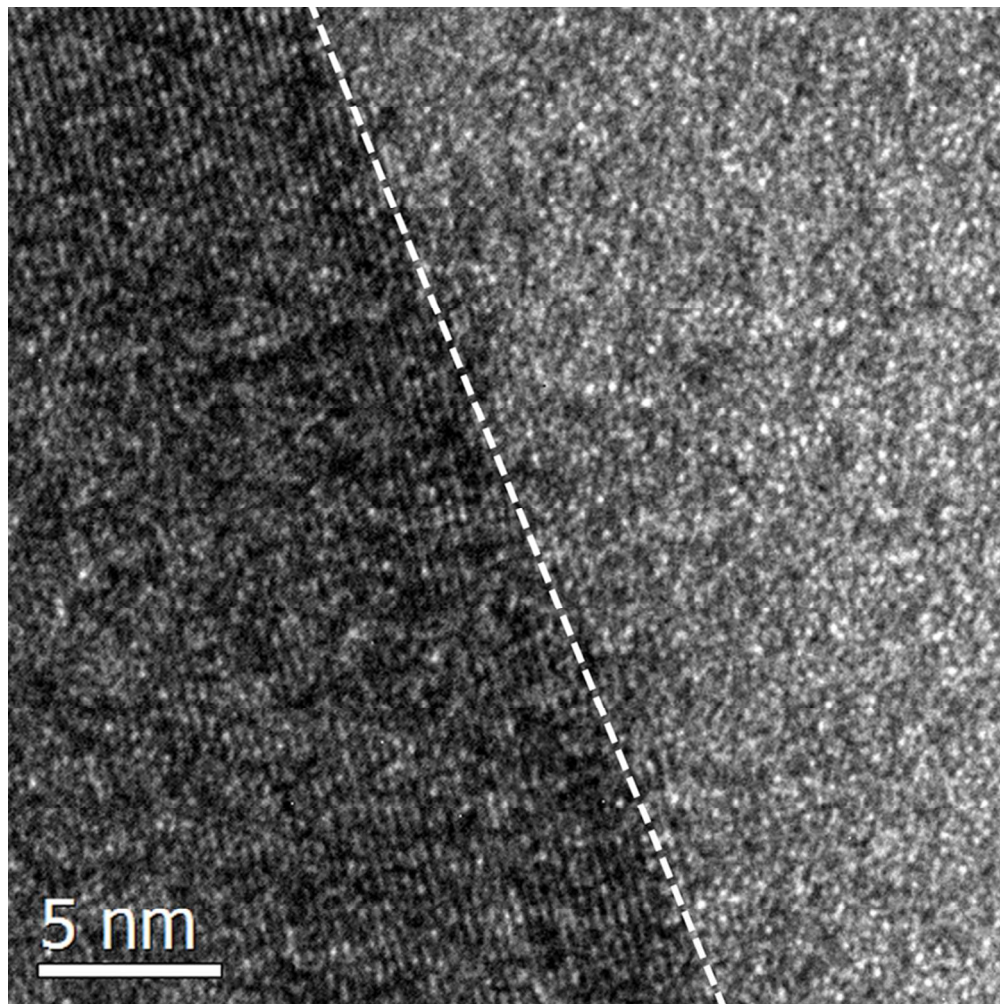


Fig. 13 (d) HR-TEM image of the crystalline and amorphous regions (marked by arrows B in Fig. 13 (a))
70x70mm (300 x 300 DPI)

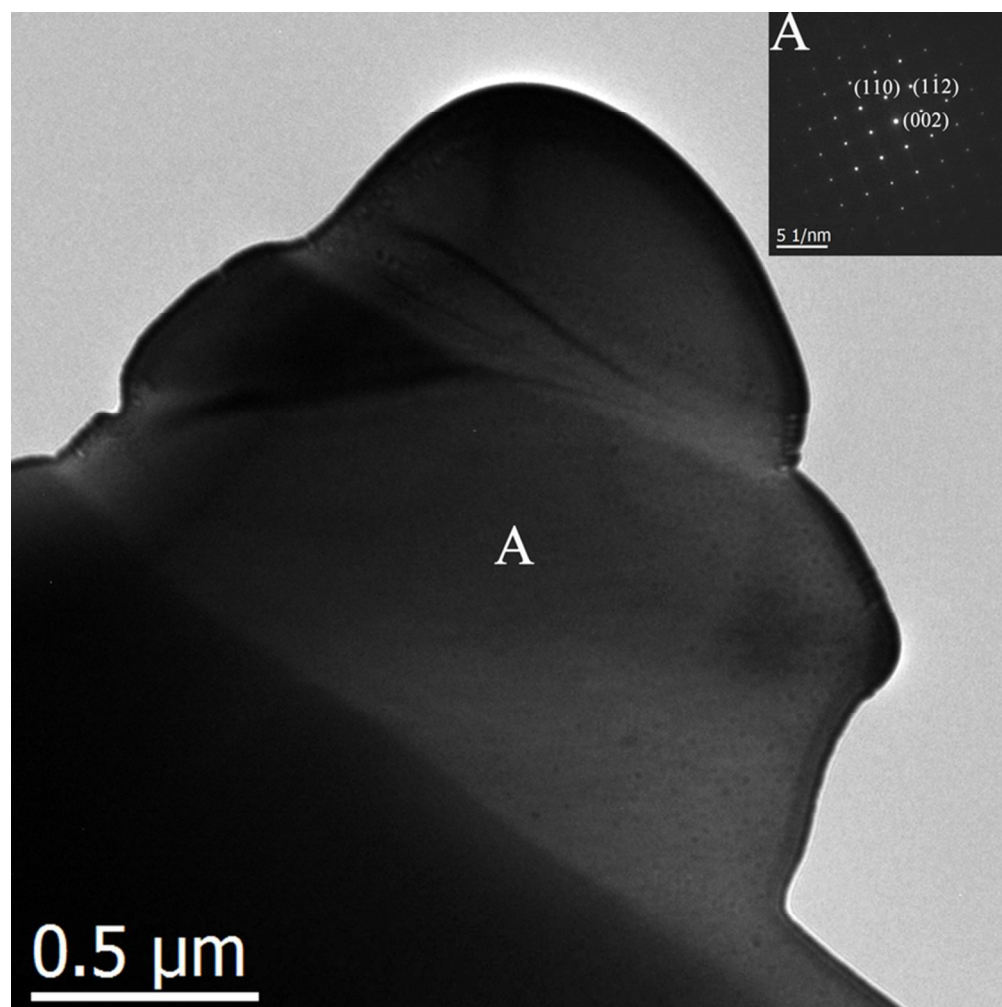


Fig. 14 (a) TEM image (bright-field image of the region without Ga evaporation) of the cross-section of the as-sprayed LSMG electrolyte prepared by powder A
70x70mm (300 x 300 DPI)

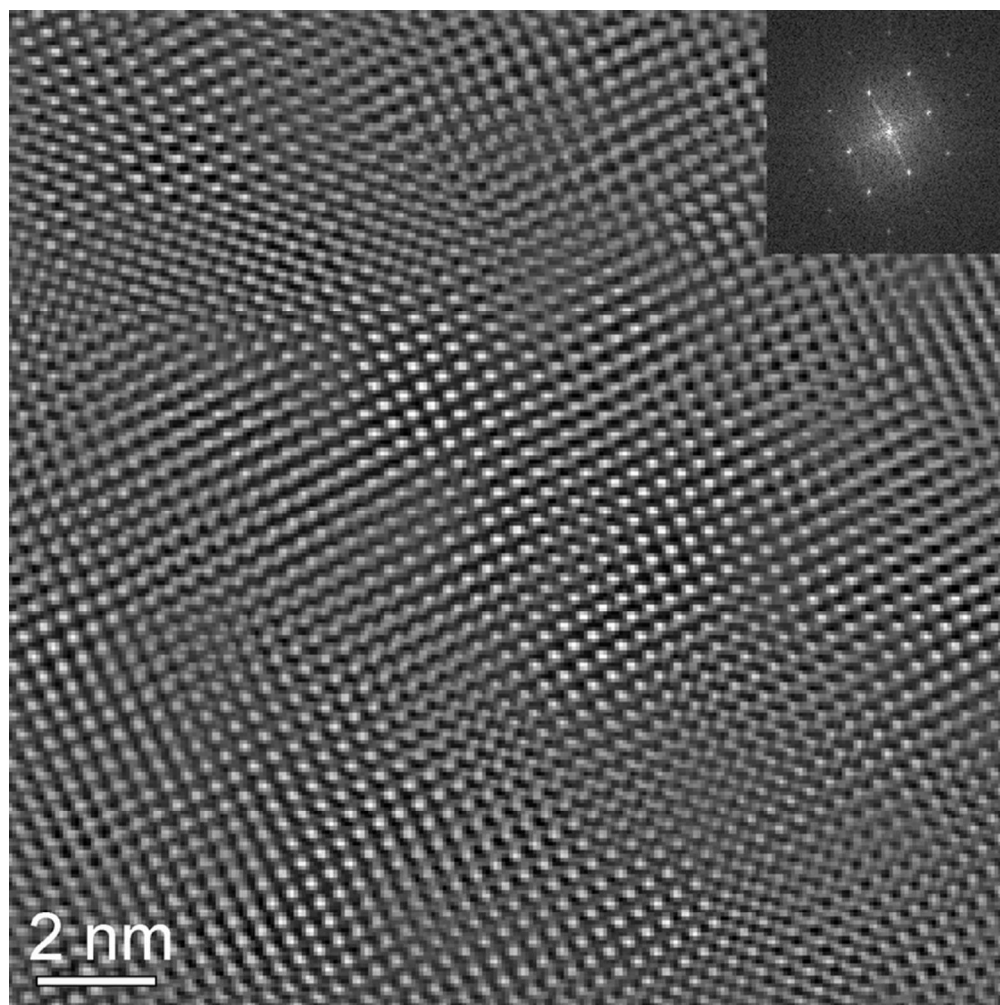


Fig. 14 (b) Electron diffraction image of the region marked as A in Fig. 14 (a)
70x70mm (300 x 300 DPI)

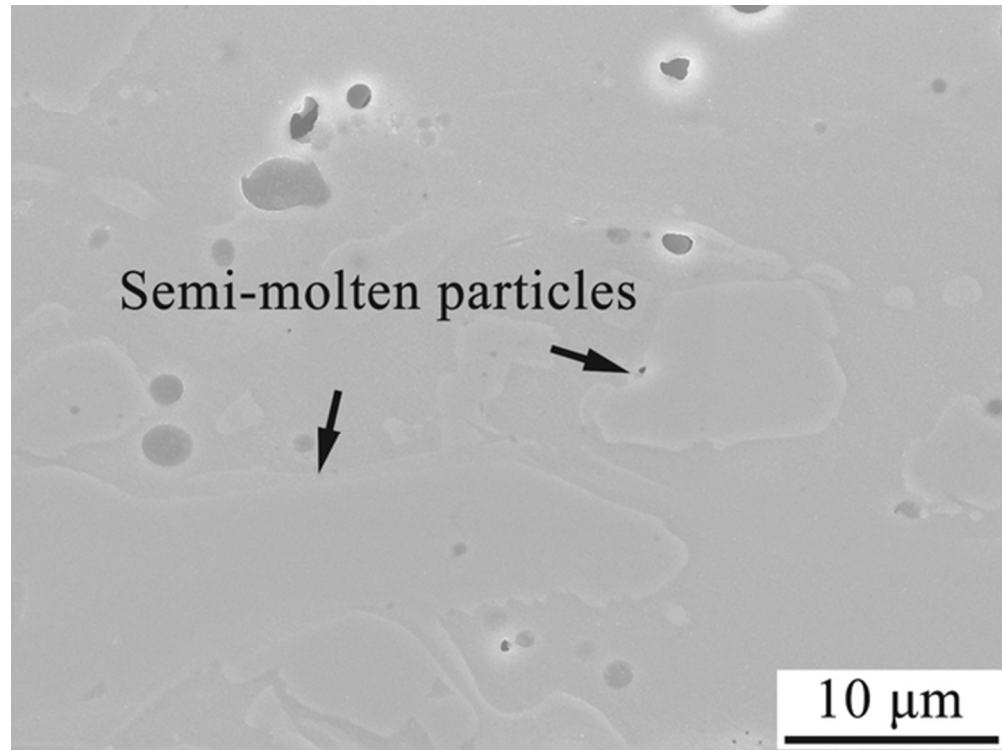


Fig. 15 (a) Microstructures of the polished cross-section of the as-sprayed LSGM deposits prepared by powder B with a size of $>30\ \mu\text{m}$
52x39mm (300 x 300 DPI)

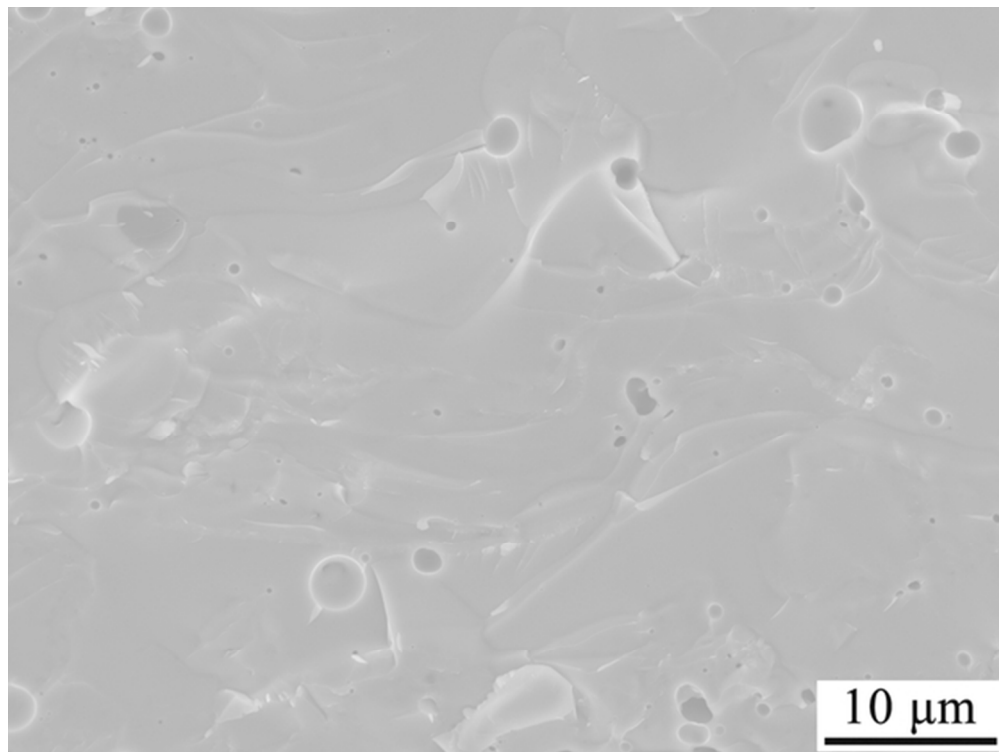


Fig. 15 (b) Microstructures of the fractured cross-section of the as-sprayed LSGM deposits prepared by powder B with a size of $>30 \mu\text{m}$
52x39mm (300 x 300 DPI)

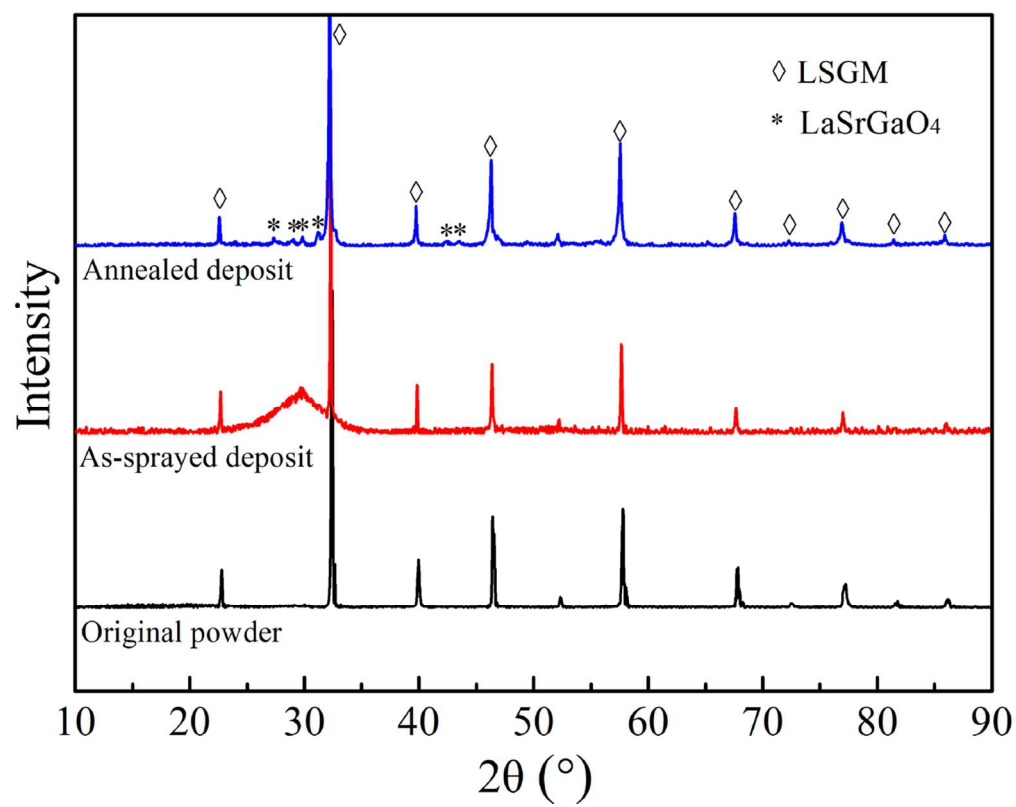


Fig. 16 (a) XRD patterns of LSGM electrolytes prepared by powder A
55x44mm (600 x 600 DPI)

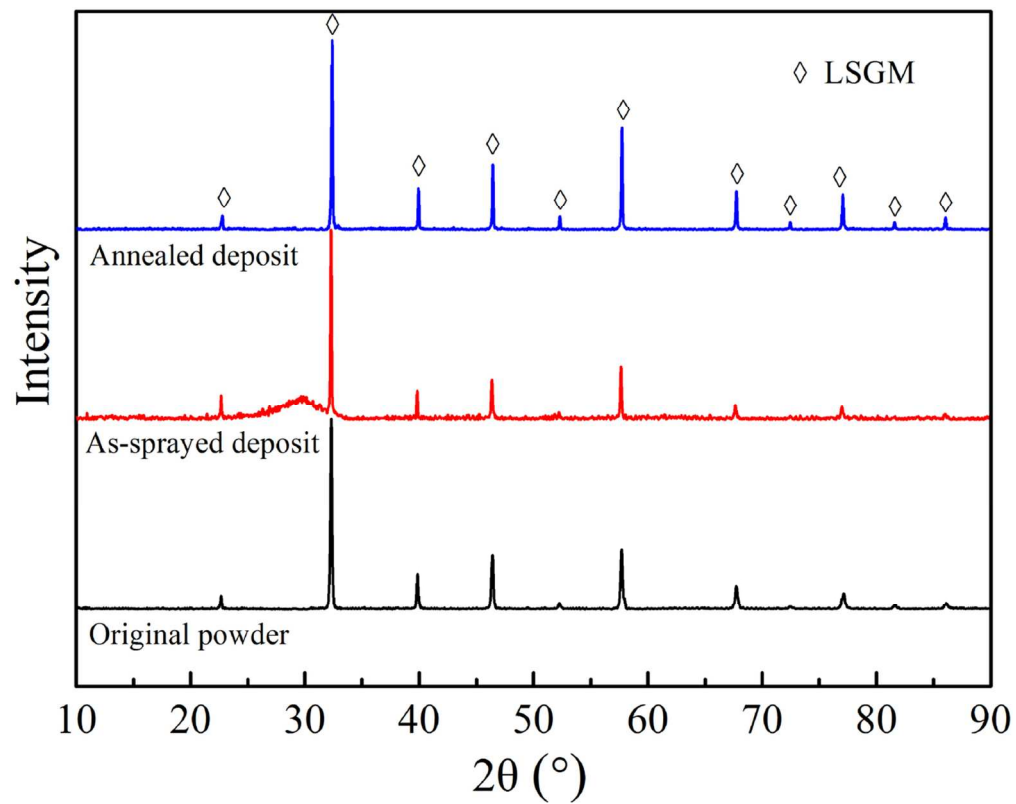


Fig. 16 (b) XRD patterns of LSGM electrolytes prepared by powder B
55x44mm (600 x 600 DPI)

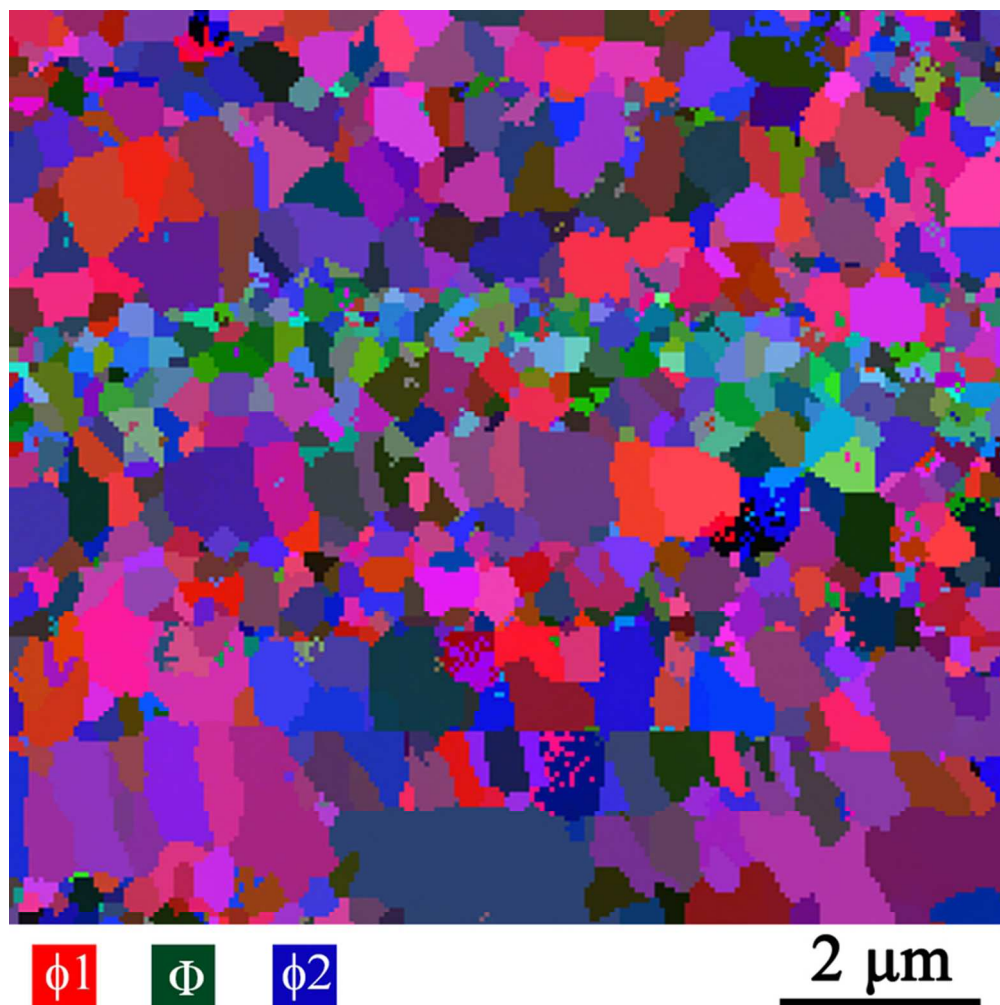


Fig. 17 (a) EBSD orientation map of Euler angle for annealed LSGM deposit
70x70mm (300 x 300 DPI)

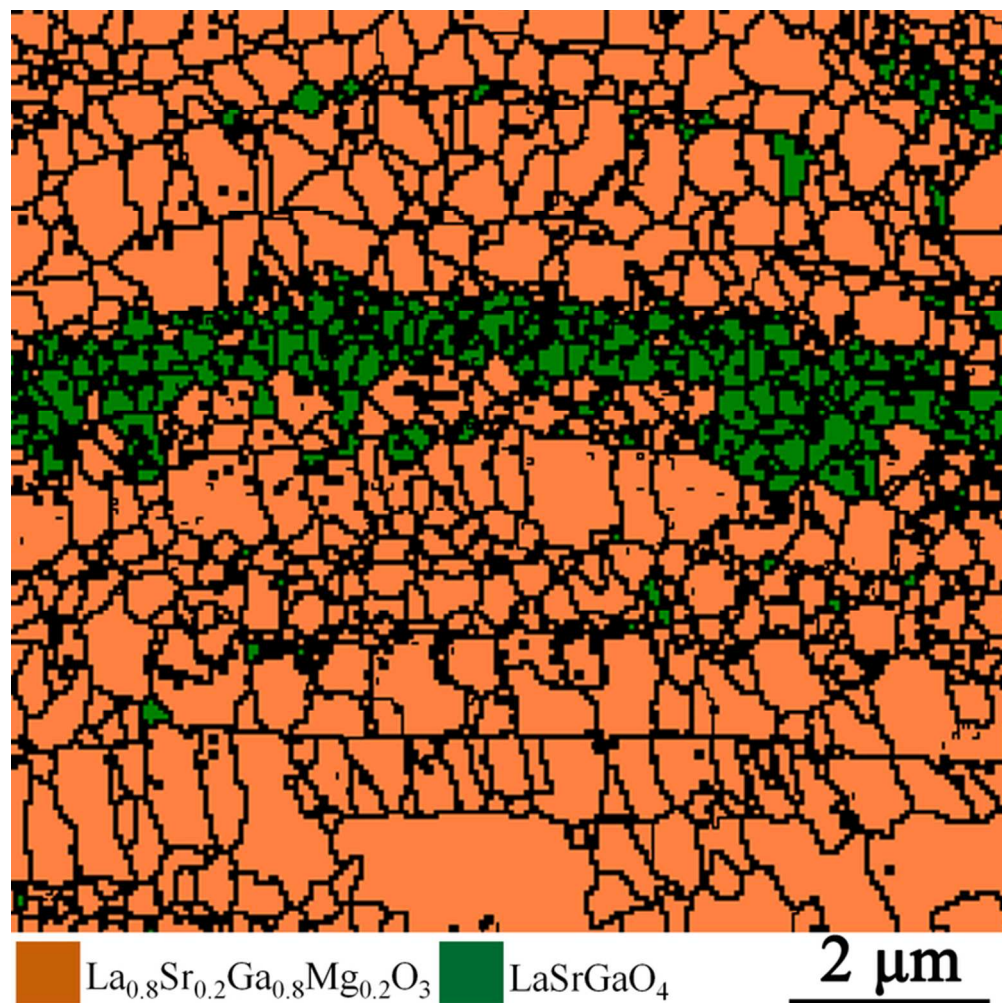


Fig. 17 (b) EBSD phase distribution map for annealed LSGM deposit
70x70mm (300 x 300 DPI)

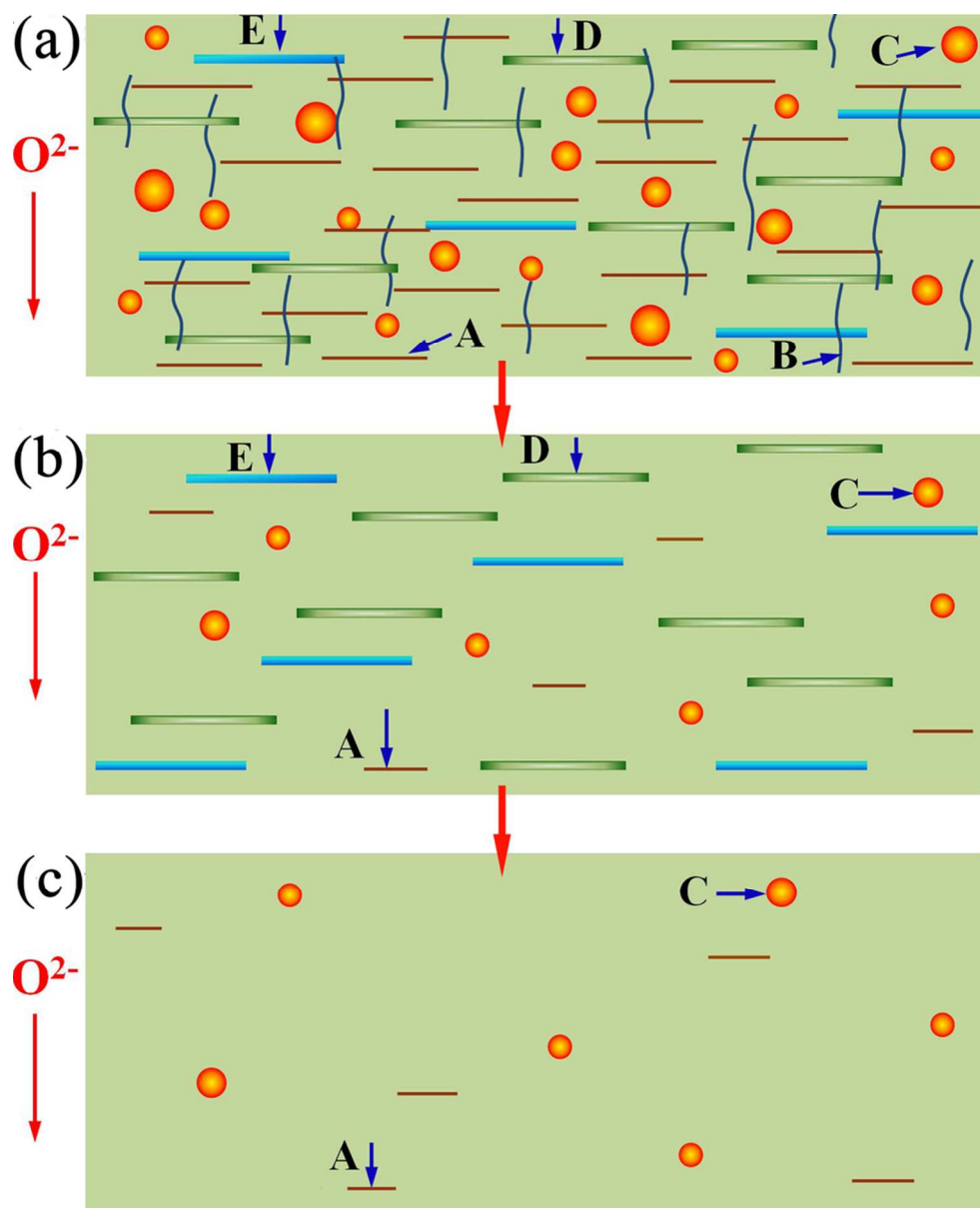


Fig. 18 Schematic diagram of the microstructural developments of plasma sprayed LSGM electrolyte by different spraying routes. (a) deposited from powder A without preheating, (b) deposited from powder A with preheating, (c) deposited from powder B with preheating. A is nonbonded interface, B is vertical cracks, C is closed pores, D is the Ga-evaporated region, and E is the LaSrGaO₄ phase
85x105mm (300 x 300 DPI)

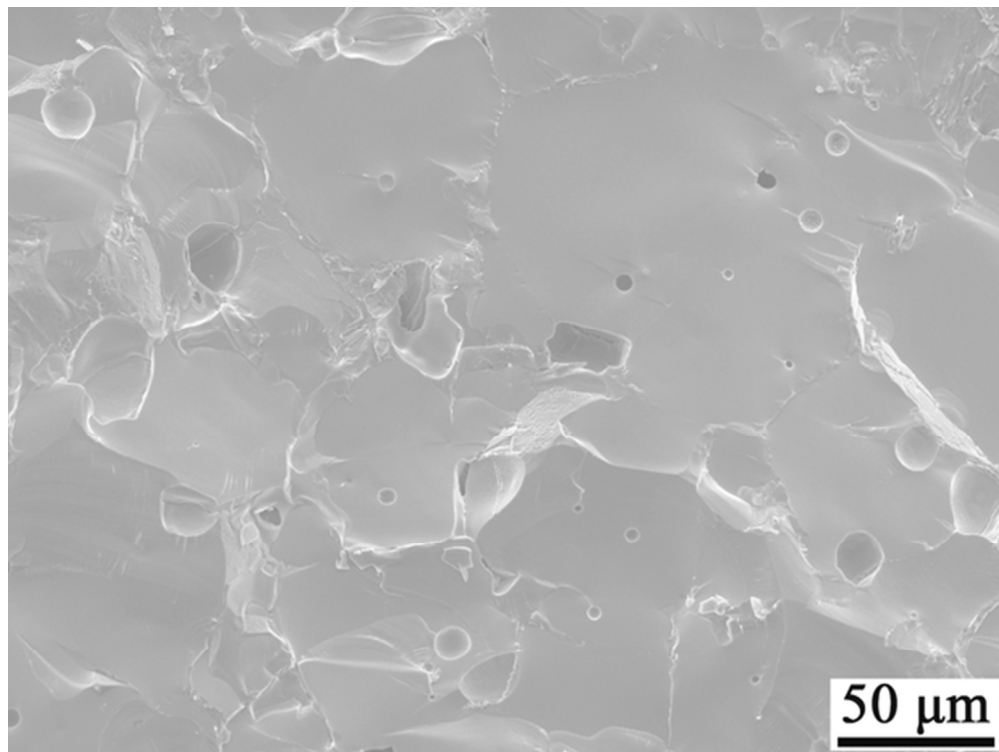


Fig. 19 (a) Morphologies of the fractured cross-section of sintered LSGM bulk 52x39mm (300 x 300 DPI)

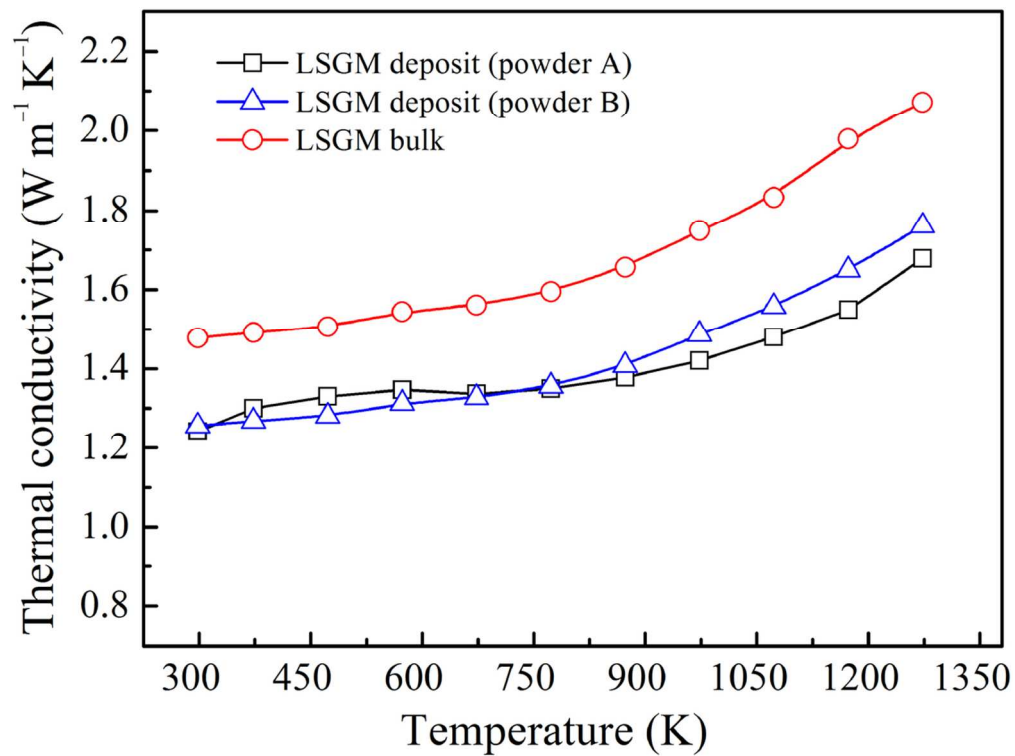


Fig. 19 (b) Thermal conductivities of LSGM bulk and deposits
52x39mm (600 x 600 DPI)

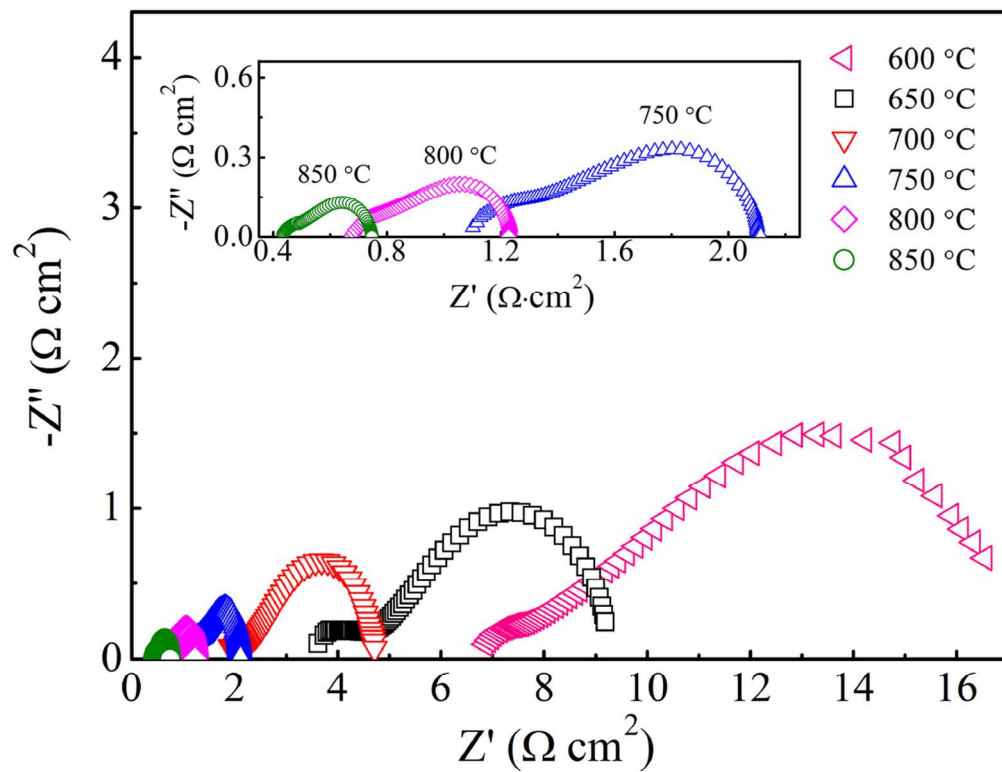


Fig. 20 (a) Electrochemical impedance spectra for sintered bulk at different temperatures
53x40mm (600 x 600 DPI)

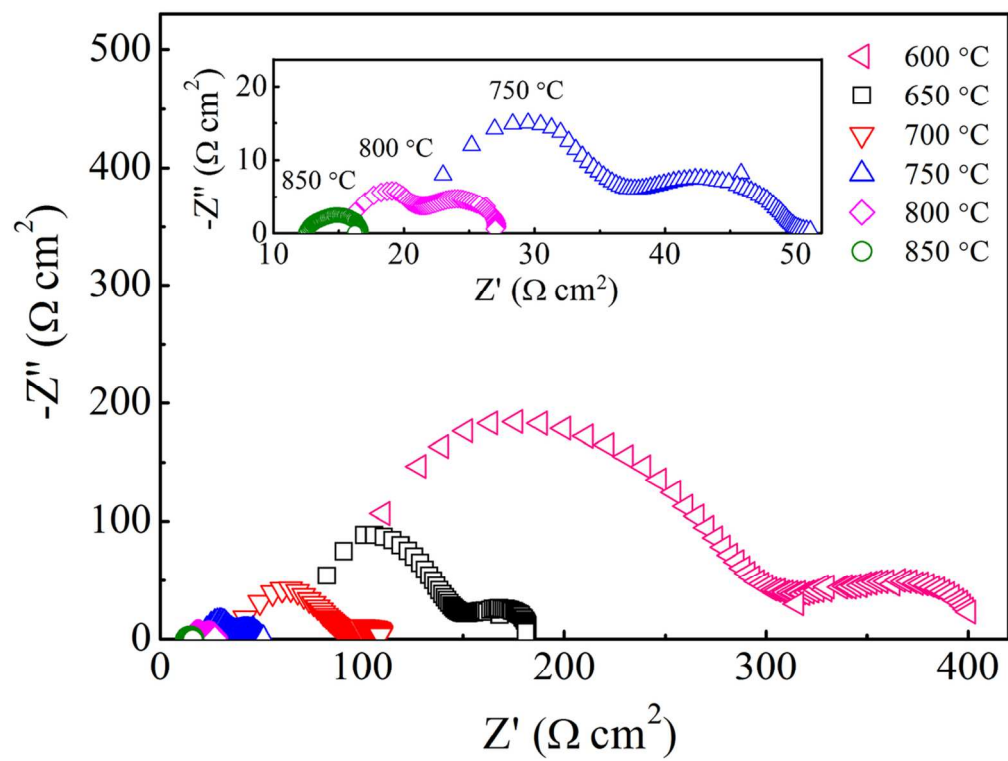


Fig. 20 (b) Electrochemical impedance spectra for deposits prepared by powder A at different temperatures
53x40mm (600 x 600 DPI)

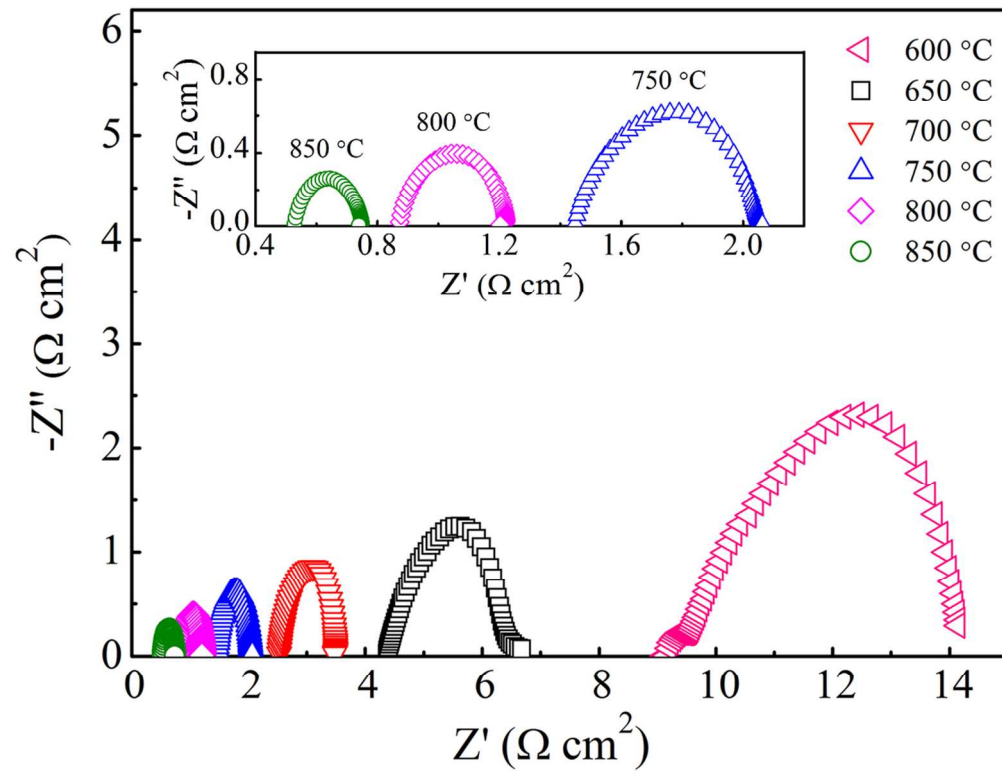


Fig. 20 (c) Electrochemical impedance spectra for deposits prepared by powder B at different temperatures
53x40mm (600 x 600 DPI)

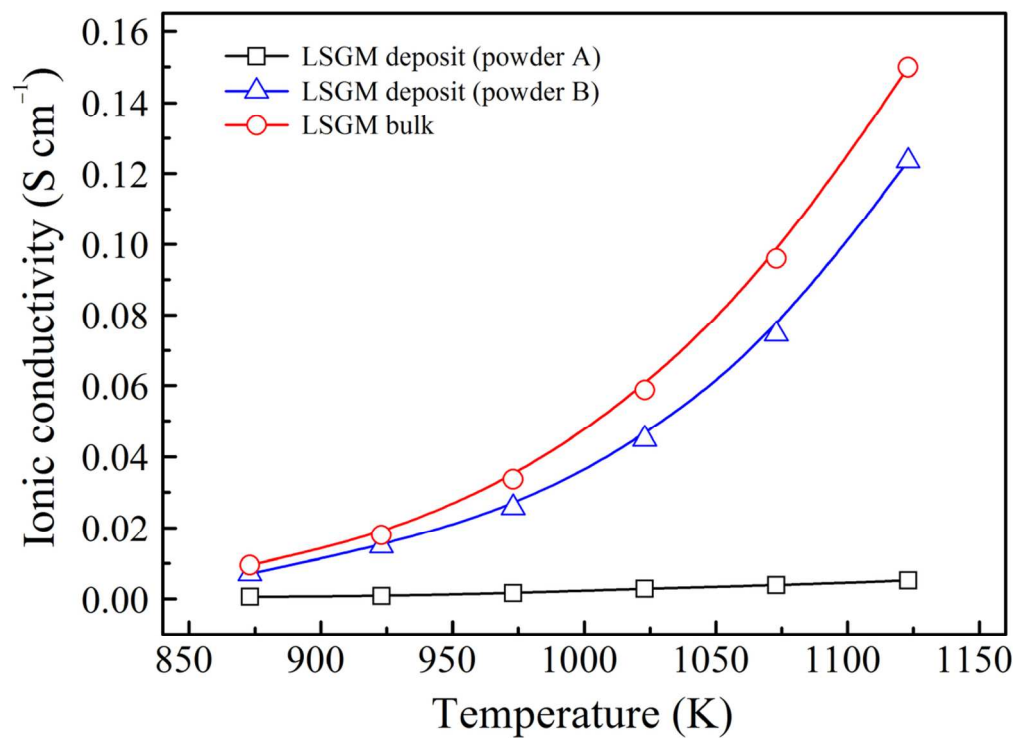


Fig. 21 (a) Total ionic conductivity of LSGM bulk and deposits
51x37mm (600 x 600 DPI)

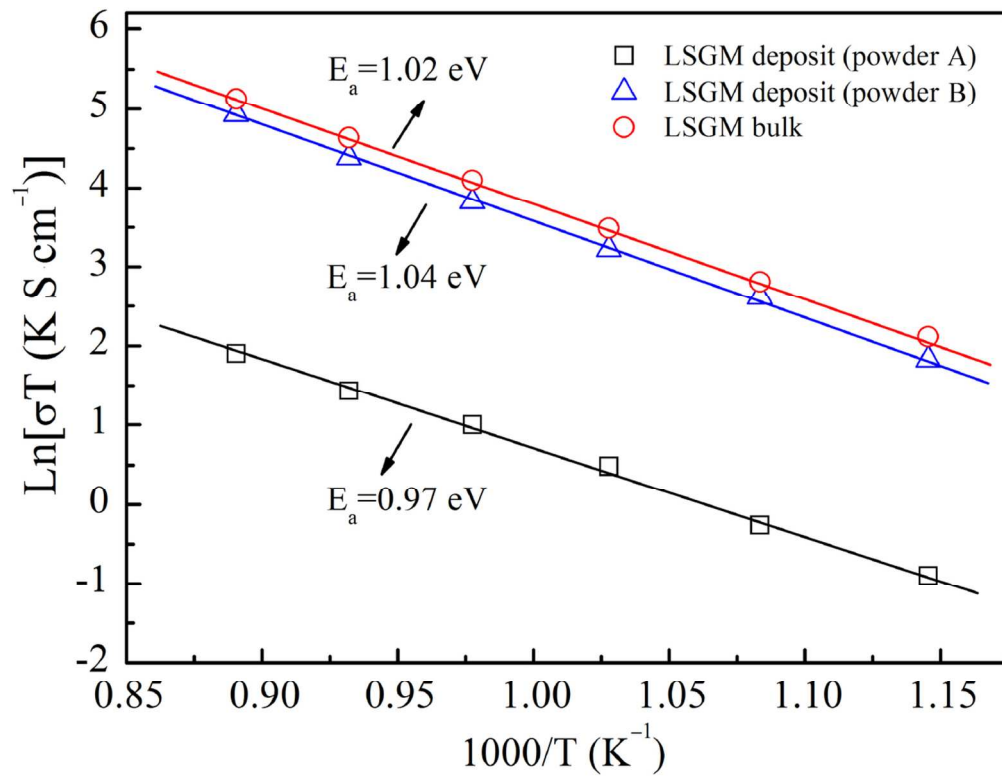


Fig. 21 (b) Arrhenius plots of the total conductivity for LSGM bulk and deposits
53x41mm (600 x 600 DPI)

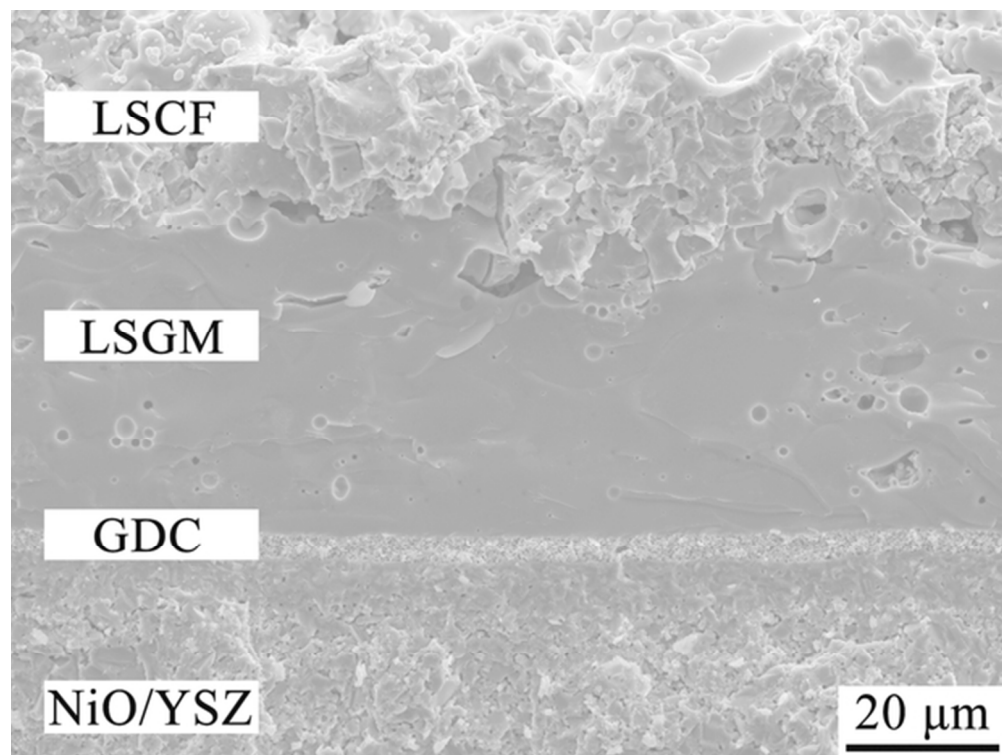


Fig. 22 (a) Cross-section of the fractured SOFC single cell
52x39mm (300 x 300 DPI)

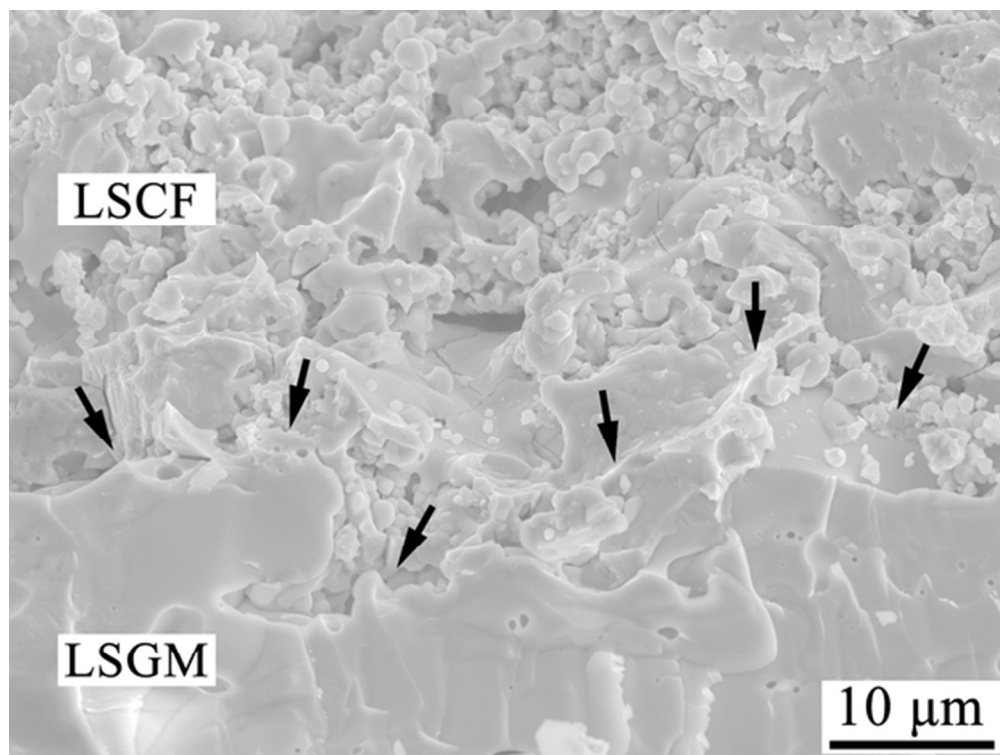


Fig. 22 (b) Microstructure of plasma-sprayed LSCF cathode and the interface between cathode and electrolyte
52x39mm (300 x 300 DPI)

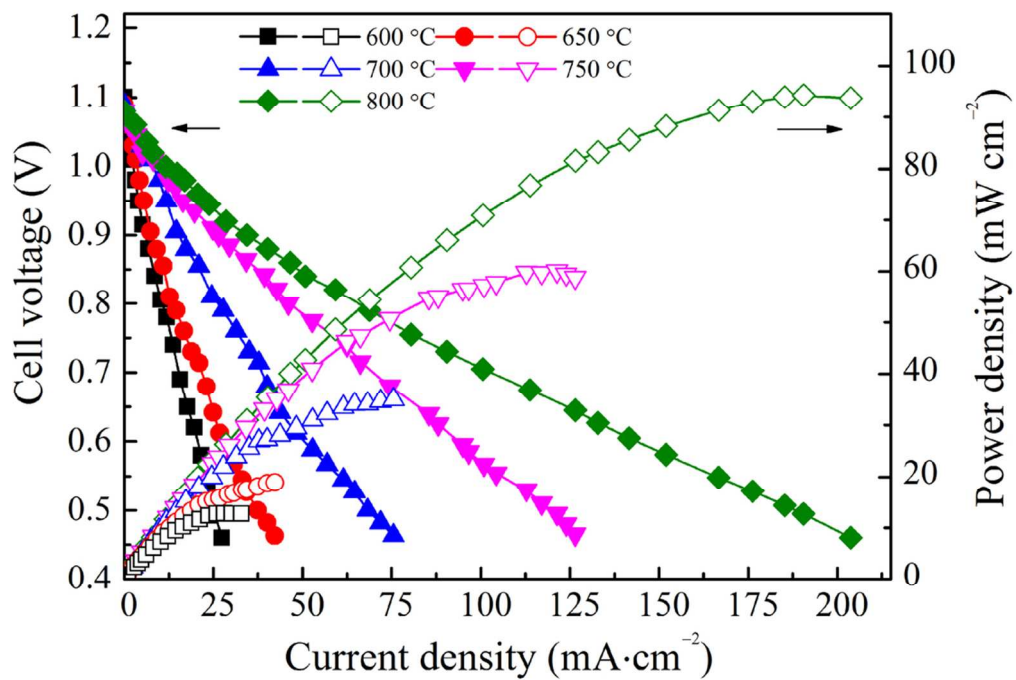


Fig. 23 (a) Output performance of the single cell with the electrolyte prepared by powder A 46x31mm (600 x 600 DPI)

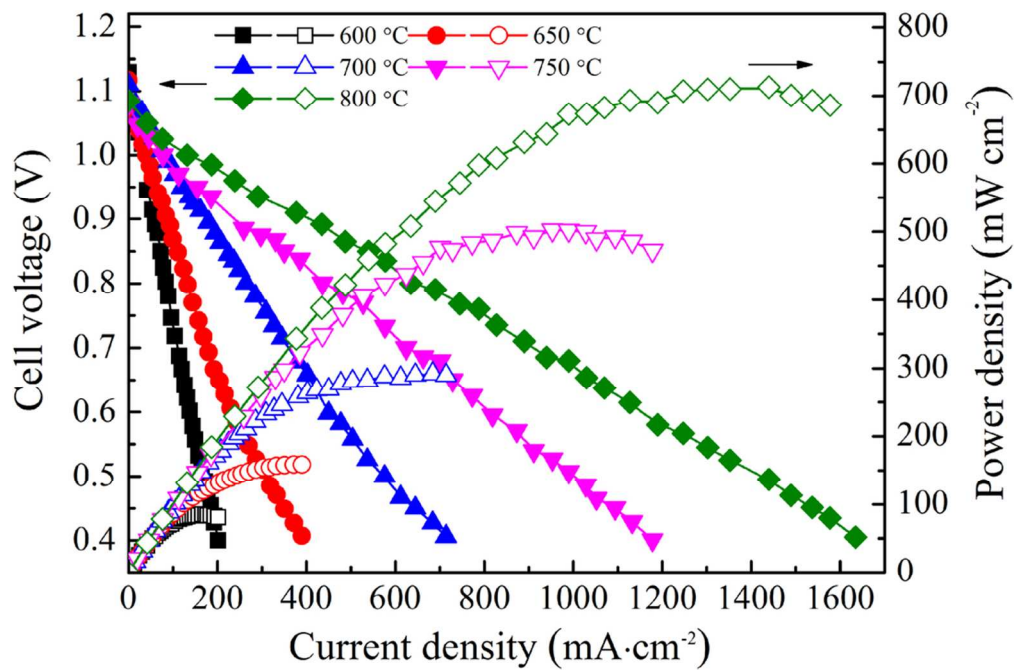


Fig. 23 (b) Output performance of the single cell with the electrolyte prepared by powder B 46x30mm (600 x 600 DPI)

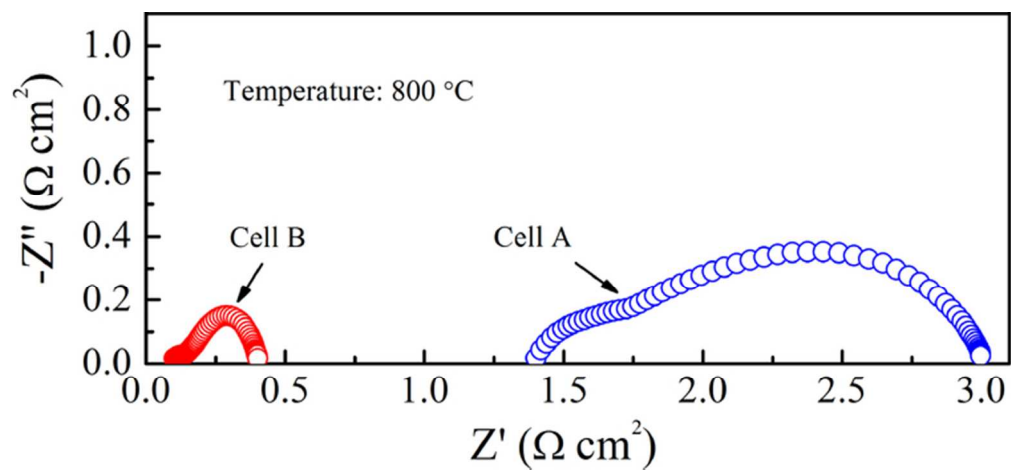


Fig. 23 (c) Impedance spectra obtained for the cells at 800 °C under the OCV conditions 31x14mm (600 x 600 DPI)

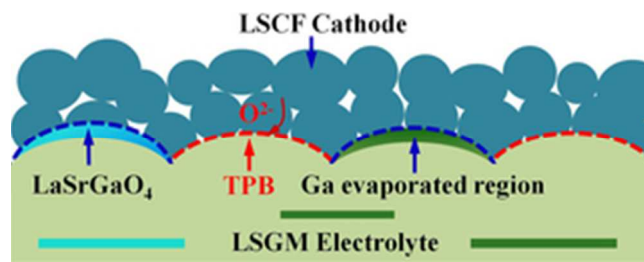


Fig. 24 (a) Schematic diagrams for the interfaces and TPBs between cathode and electrolytes prepared by powder A
27x10mm (300 x 300 DPI)

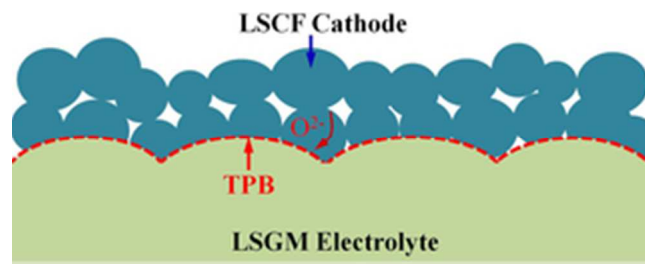


Fig. 24 (b) Schematic diagrams for the interfaces and TPBs between cathode and electrolytes prepared by powder B
27x10mm (300 x 300 DPI)